OBSERVATIONS D'ONDES INTERNES SOLITAIRES PRÈS D'UN QUAI ET LEUR POTENTIEL IMPACT SUR LA NAVIGATION

MÉMOIRE PRÉSENTÉ
dans le cadre du programme de maîtrise en océanographie
en vue de l'obtention du grade de maître ès sciences

PAR
©LOUIS HUPÉ

Décembre 2025

Composition du jury :

Dany Dumont, président du jury, Université du Québec à Rimouski

Daniel Bourgault, directeur de recherche, Université du Québec à Rimouski

Cédric Chavanne, codirecteur de recherche, Université du Québec à Rimouski

Sandy Grégorio, codirectrice de recherche, Université du Québec à Rimouski

Jacqueline McSweeney, examinatrice externe, Stony Brook University

Dépôt initial le 07 octobre 2025 Dépôt final le 18 décembre 2025

UNIVERSITÉ DU QUÉBEC À RIMOUSKI
Service de la bibliothèque

Avertissement

La diffusion de ce mémoire ou de cette thèse se fait dans le respect des droits de son auteur, qui a signé le formulaire « *Autorisation de reproduire et de diffuser un rapport, un mémoire ou une thèse* ». En signant ce formulaire, l'auteur concède à l'Université du Québec à Rimouski une licence non exclusive d'utilisation et de publication de la totalité ou d'une partie importante de son travail de recherche pour des fins pédagogiques et non commerciales. Plus précisément, l'auteur autorise l'Université du Québec à Rimouski à reproduire, diffuser, prêter, distribuer ou vendre des copies de son travail de recherche à des fins non commerciales sur quelque support que ce soit, y compris l'Internet. Cette licence et cette autorisation n'entraînent pas une renonciation de la part de l'auteur à ses droits moraux ni à ses droits de propriété intellectuelle. Sauf entente contraire, l'auteur conserve la liberté de diffuser et de commercialiser ou non ce travail dont il possède un exemplaire.

REMERCIEMENTS

Ces deux années de maîtrise à Rimouski ont été une chance formidable. J'aimerais tout d'abord remercier ma direction de recherche, Daniel, Sandy et Cédric. Avec mon double parcours d'étudiant-athlète, ils ont toujours su me donner assez de liberté pour que je puisse m'épanouir dans les deux domaines. J'ai aussi eu grâce à eux l'opportunité de participer deux fois à la Réunion Scientifique Annuelle de Québec Océan et à l'European Geoscience Union à Vienne. Que rêver de plus pour commencer une carrière scientifique ? Votre professionnalisme et votre proximité (je n'oserais plus jamais vous vouvoyer ;-)) m'ont permis de grandir et de gagner en maturité, pour rentrer sereinement dans le monde du travail ou du doctorat. Vous m'avez aussi permis de travailler avec nos propres données récoltées à l'automne 2023 et à l'été 2024 dans le fjord du Saguenay. J'aimerais remercier Peter et Jean-Luc pour leur présence et aide à ces campagnes. Faire un transect presque entier du fjord entourés de bélugas, marsouins et phoques est l'expérience d'une vie ! Nous n'aurions pas eu autant de données aussi grâce au prêt d'équipements pour les mouillages d'Urs Neumeier (ISMER) et à l'aide de Julien Vadnais (University of Bergen) pour son expertise et son aide à retrouver des images SAR. Les aides de Port Saguenay, de l'Administration de pilotage des Laurentides, d'Alain Richard—Expert Nautique, de Pêches et Océans Canada et de Québec Océan ont aussi permis à ce projet de voir le jour. Merci !

Ce mémoire n'en serait pas un sans son président du jury, Dany Dumont (ISMER) et sa membre externe, Jacqueline McSweeney (Stony Brook University). Merci Dany d'avoir accepté cette présidence, tu as toujours pu m'aider quand j'avais des questions sur la maîtrise ou sur des opportunités de travail. Thank you, Jacqueline, for agreeing to be part of this master's thesis. I really enjoyed our previous conversations about your research and your cheerfulness. Despite the distance, you have always been helpful, especially when I was trying to find PhD opportunities in the U.S. before the new policies. Thank you again !

Je veux remercier aussi tous les membres du POLR. Que ça soit Rosalie pour les pauses mots-croisés, Maria pour ta date d'anniversaire dure à oublier, Margaux pour les discussions sur le Lot-et-Garonne, Xavier pour les fiches d'impôts ou Christophe pour ton sirop d'érable et ta viande d'orignal, un grand merci ! Je ne peux pas aussi faire des remerciements en omettant Jérôme. Ta patience, ta présence et même ta pédagogie m'ont permis de parler le Matlab, de parler aux données et de parler aux images géoréctifiées. Ton aide a été sincèrement inestimable au cours de ces deux ans. T'as déchiré !

Ces deux ans m'ont permis de faire des rencontres. Merci Marie, Manon, Tommy-Loup, Juan, Daphnée, Clément, Amélie, Achraf et j'en oublie pour votre amitié et votre confiance ! Merci à toi Vincent, première personne rencontrée à l'ISMER, tu m'as rapidement fait découvrir la Boulatek. Que serait une promenade à la réserve faunique sans ta datation des nuggets d'orignal ? Merci à toi Dr. Julie, d'avoir été comme une grande sœur à qui on peut toujours tout confier. Par contre tes lasagnes sont un peu sèches, tu devrais écouter Vincent. Merci à toi Nina, d'avoir toujours bien voulu être le personnage secondaire du groupe avec moi. Il faudrait juste te mettre au vrai gaming !

Merci aussi à ma famille montréalaise, les Portelance, ma famille haligonienne, les Anderson et à Sue et Ali pour leur hospitalité alors que j'étais un inconnu. Je n'oublierai jamais la manière dont vous m'avez accueilli et j'espère vous voir à la maison un jour !

Enfin, j'aimerais remercier toute ma famille pour leur affection, leur soutien et leurs conseils. Sans cet esprit de famille, qui sait si j'aurais un jour quitté la maison pour La Rochelle, Marseille, Rimouski et maintenant Halifax ? Vous m'aidez à aspirer à devenir une meilleure personne, du fond du cœur merci ! Ce mémoire est un peu le vôtre aussi.

RÉSUMÉ

Cette recherche est motivée par un incident survenu dans le fjord du Saguenay (QC, Canada) en 2019, où un cargo est entré en collision avec un quai lors de son accostage, entraînant des dommages matériels mineurs tant au navire qu'au quai dans des circonstances mal comprises au moment de l'incident. Notre hypothèse est que des ondes internes solitaires ont pu contribuer au déplacement du navire. Pour tester cette hypothèse, des sondes CTD, des ADCPs, des caméras et un échosondeur ont été déployés durant l'été 2024. Les deux semaines d'échantillonnage ont révélé la présence d'ondes internes solitaires. Ces observations montrent que des trains d'ondes internes ont heurté presque quotidiennement le quai et qu'elles semblent être en phase avec le cycle de marée. Des ondes internes d'une longueur d'onde de 60 m et d'une période de 40 s ont été enregistrées avec des amplitudes pouvant atteindre 10 m et des courants horizontaux associés de l'ordre de 1 $\mathrm{m\,s^{-1}}$. Ces courants semblent suffisamment forts pour affecter la manœuvrabilité d'un cargo lors de l'accostage. Les résultats de cette recherche pourraient contribuer à l'amélioration des simulateurs de navigation, en prenant en compte les effets des ondes internes sur les manœuvres d'accostage.

Mots clés : Ondes internes, marées, fjord, navigation, accident

ABSTRACT

This research is motivated by an incident in the Saguenay Fjord (QC, Canada) that occurred in 2019, where a cargo ship collided with a wharf while docking, resulting in minor material damage to both the vessel and the wharf under circumstances that remain unknown at the incident's moment. Our hypothesis is that internal solitary waves may have contributed to the ship's displacement. To test this hypothesis, CTDs, ADCPs and an echosounder were deployed during the summer of 2024. The two-week sampling period revealed the presence of internal waves on an almost daily basis. These observations show that trains of internal waves impacted the wharf daily and that they appear to be phase-locked with the tidal cycle. Internal waves of a wavelength of 60 m and period of 40 s were recorded with amplitudes reaching 10 m and wave-induced horizontal currents up to 1 $\mathrm{m\,s^{-1}}$. These currents are potentially strong enough to affect the maneuverability of a cargo ship during docking. The results of this research could contribute to the improvement of navigation simulators by enabling them to account for the effects of internal waves on docking maneuvers.

Keywords : Internal waves, tides, fjord, navigation, accident

TABLE DES MATIÈRES

LISTE DES FIGURES

INTRODUCTION GÉNÉRALE

Avec la mondialisation, les échanges commerciaux par voie maritime n'ont jamais été aussi importants. Cette intensification expose les cargos à de nouveaux défis, notamment ceux liés à leur sécurité et leur manœuvrabilité dans les ports. Anticiper le vent, les vagues ou les courants de surface est essentiel pour des opérations portuaires plus sûres et rapides. Toutefois, les aléas maritimes ne se limitent pas à ces forces de surface. Des paramètres comme la température et la salinité contrôlent la structure de la colonne d'eau et conditionnent des courants qui peuvent créer des risques pour les activités en mer (Osborne and Burch, 1980).

Les océans sont divisés en plusieurs couches avec des eaux denses en profondeur et des eaux moins denses en surface. Bien que la densité des eaux est variable d'un endroit à l'autre sur le globe, cette répartition est particulièrement marquée dans les milieux estuariens et fjordiens où se rencontrent des eaux maritimes salées et des eaux fluviales douces (Geyer and MacCready, 2014). On appelle pycnocline l'interface qui sépare les eaux denses profondes des eaux moins denses de surface. La pycnocline délimite deux milieux de densités différentes de la même manière que l'interface air-mer. D'une façon comparable au développement de vagues à la surface de l'océan, la pycnocline, lorsque perturbée, peut se développer en ondes communément appelées ondes internes ou vagues sous-marines. Dans les fjords et estuaires, ces vagues sous-marines peuvent atteindre une dizaine de mètres d'amplitude avec une longueur d'onde de plusieurs dizaines de mètres, et se déplacer avec une vitesse de propagation d'environ 1 $\mathrm{m\,s^{-1}}$.

Dans les estuaires et les fjords, la colonne d'eau est généralement divisée en deux couches d'eau. Une onde interne adoptera un caractère différent selon l'épaisseur relative de ces couches. Dans un système où la couche de surface est plus mince que la couche de fond, l'onde interne adoptera une forme de cloche inversée. On parle alors d'une onde de dépression (figure 1). Dans le cas contraire où la couche de fond est plus mince que la couche de surface, l'onde interne adoptera une forme de cloche ou de gaussienne. On parle alors d'une onde d'élévation (figure 2). Les deux types d'ondes sont observés dans les océans et les milieux côtiers. Cependant, dans ce mémoire il sera essentiellement question d'ondes de dépression qui se propagent à quelques mètres de la surface.

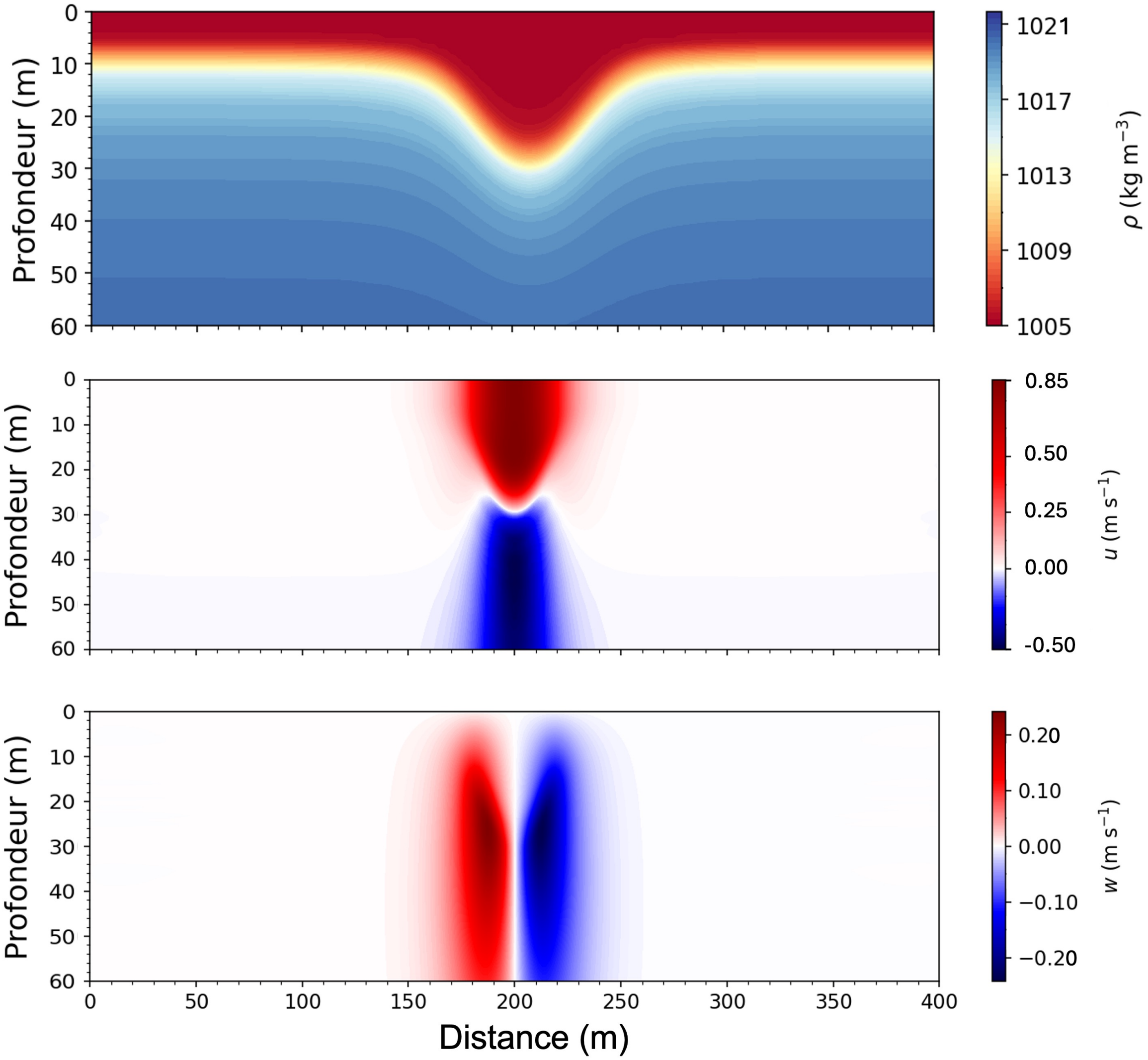

FIGURE 1 – Masse volumique, ρ, vitesses horizontale, u, et verticale, w, d'une onde interne de dépression calculée selon la théorie de Dubreil-Jacotin-Long (DJL) (Stastna and Lamb, 2002) avec le solveur Python DJLES (Dunphy et al., 2011).

Lorsque les ondes internes sont dites solitaires, chaque onde d'un train d'ondes a une vitesse et une amplitude qui lui est propre. Aussi, si elle ne rencontre pas d'obstacle, ni de variation des conditions ambiantes de stratification et de courant, l'onde interne solitaire gardera la même forme tout au long de sa propagation. Dans un train d'ondes internes solitaires (OIS) idéalisé, la première onde sera la plus grande et la plus rapide, tandis que la dernière sera la plus petite et la plus lente. En effet, la vitesse de l'onde augmente avec son amplitude (Osborne and Burch, 1980). Les courants associés aux OIS sont caractérisés par des mouvements horizontaux convergents et divergents, ce qui entraîne des courants descendants dans les zones convergentes, et, ascendants dans les zones divergentes. Dans les zones convergentes, de légères modifications de la rugosité de la surface de l'eau modifient la réflectance de celle-ci, créant des stries qui constituent une signature de surface propre aux ondes internes (Osborne and Burch, 1980) (figure 3). Ainsi, malgré leur nature sous-marine, il est possible de les détecter par voie aérienne ou satellitaire lorsque les conditions de mer et de vent sont calmes. On retrouve les OIS partout dans les milieux océaniques (Jackson and Apel, 2004), notamment dans le fjord du Saguenay (Bourgault et al., 2016).

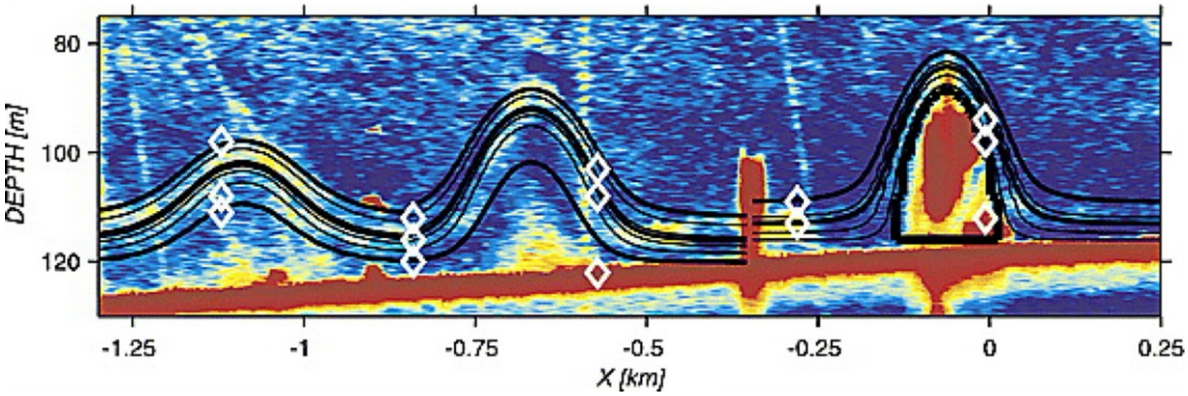

FIGURE 2 – Train d'ondes internes d'élévation observé au large de l'Oregon (É-U). Les courbes noires représentent les isopycnes (Klymak and Moum, 2003).

FIGURE 3 – Signature de surface d'un train d'OIS s'approchant du quai de Grande-Anse (QC, Canada) le 27 septembre 2023 (Grégorio et al., 2025). On remarque bien l'alternance de stries claires et foncées en surface propre aux OIS.

Les sources des OIS sont très variées et souvent mal comprises. Une source assez bien connue et documentée de génération d'OIS est la marée. Une masse d'eau entraînée par un courant de marée qui rencontre un obstacle topographique sous-marin peut perturber la pyncoline et ainsi générer des ondes internes (Jackson et al., 2012). On retrouve, par exemple, ce type de génération dans la mer de Chine méridionale (Alford et al., 2015). Un vent fort peut aussi générer des OIS en transmettant son énergie de la surface vers la profondeur, développant des ondes internes linéaires qui dégénèrent en OIS (Heaps and Ramsbottom, 1966; Bergh and Berntsen, 2009). Enfin, dans le fjord du Saguenay, Bourgault et al. (2016) ont montré qu'un front entre deux masses d'eau peut générer des ondes internes. Dans un front, une masse d'eau plus dense passe sous une masse d'eau moins dense. Cette intrusion crée une cisaille suffisamment forte pour déstabiliser la pycnocline, générant ainsi des instabilités de Kelvin-Helmholtz et de la turbulence. Des OIS de grande amplitude sont générées au nez de l'intrusion, s'en détachent, puis se propagent le long de la pycnocline environnante.

Historiquement, les ondes internes ont surtout été étudiées de manière fondamentale. Cependant, il existe quelques évènements qui laisseraient penser que les vagues sous-marines pourraient affecter la navigation. Par exemple, Osborne et al. (1978) ont montré que les vagues sous-marines ont un impact sur les navires, notamment sur les navires de forage. La ligne d'ancrage ainsi que le train de tiges du bateau sont soumis à la force des ondes qui exerce une certaine tension. L'étude conclut que, bien qu'il n'y ait eu aucun accident dans l'unique cas étudié, les vagues sous-marines sont à prendre en compte pour l'exploitation pétrolière offshore. Depuis les années 1980, il est possible que les vagues sous-marines aient provoqué des accidents. En 1984, un sous-marin nucléaire soviétique a brusquement émergé dans le détroit de Gibraltar, percutant un navire de surface et causant des dégâts importants au submersible (Osborne, 2010). Le détroit de Gibraltar est une zone connue pour la présence régulière de vagues sous-marines (Jackson and Apel, 2004), en général provoquées par un ressaut hydraulique forcé par la marée (Richez, 1994). Il est supposé que le sous-marin ait été pris dans un train d'ondes et, par les courants ascendants associés, ait été poussé vers la surface (Osborne, 2010). Plus récemment, Gong et al. (2022) ont suggéré que des ondes internes dans le détroit de Lombok pourraient être à l'origine du naufrage d'un sous-marin de la marine indonésienne. Il est possible que le submersible ait été pris dans un train d'ondes et emmené à environ 200 m de profondeur au-delà de la tolérance de pression du sous-marin par les courants descendants associés aux ondes. Cette descente aurait conduit à l'implosion du sous-marin. Comme il n'existe pas de données *in situ* de la zone le jour du naufrage, il est toutefois impossible de valider cette hypothèse. Enfin, Watson et al. (1992), Thompson and Jensen (1993) et Grue et al. (2016) ont montré que certains navires sont capables de générer leur propres ondes internes en naviguant, ce qui montre que ce phénomène n'est pas uniquement d'origine naturelle. Il est ainsi possible que les ondes internes générées par l'avancée du cargo le rattrapent au moment de son accostage (Grégorio et al., 2025). Finalement, seul Ghomsi (2015) a attribué la casse d'une haussière de mouillage d'un navire pétrolier dans le golfe de Guinée au passage d'ondes internes particulièrement fortes.

Ici, nous sommes motivés par un événement survenu en 2019 au terminal maritime de Grande-Anse à Saguenay (QC, Canada). Le soir du 30 septembre, alors que le cargo *Jaeger Arrow* entamait sa manœuvre d'accostage dans des conditions de mer calme, il a soudainement été déporté de 33 m vers le large pendant 154 s, ce qui correspond à une vitesse d'environ $0.2\ \mathrm{m\,s^{-1}}$. Le pilote s'est alors repositionné et rapproché du quai pour une seconde tentative d'accostage en prenant en compte ce courant. Environ 30 minutes après la première tentative d'accostage, le cargo, alors distant du quai de 10 m, a été déporté vers celui-ci pendant 30 s ce qui a conduit à une collision. Des dégâts matériels ont été déplorés comme le perçage du réservoir d'eaux de ballast du *Jaeger Arrow* et des dommages au quai. Les causes de l'accident demeurent inconnues pour les agents portuaires et les experts navals.

Néanmoins, d'après le déroulement et le lieu de l'accident, il est possible qu'un train d'OIS en soit à l'origine. Le mouvement oscillatoire du cargo, tantôt vers le large, tantôt contre le quai, s'accorde avec l'effet que pourrait engendrer la réflection d'un train d'ondes contre le quai. La durée de l'incident, 30 minutes, est également cohérente avec l'hypothèse qu'un train d'OIS arrive et se réfléchisse contre le quai avec une vitesse de propagation de 0.7 $\mathrm{m\,s^{-1}}$ (Grégorio et al., 2025). La stratification très marquée du fjord du Saguenay, ainsi que ses forts courants de marée sont deux éléments propices à la génération d'OIS. Enfin, nous avons récemment confirmé que des ondes internes frappent régulièrement le quai de Grande-Anse (Grégorio et al., 2025). Tous ces éléments montrent qu'il est possible que le *Jaeger Arrow* ait été déporté latéralement par des ondes incidentes et réfléchies au quai.

Pour vérifier cette hypothèse, nous avons réalisé des simulations numériques bidimensionnelles où un train d'OIS frappe le quai perpendiculairement (Grégorio et al., 2025). Il en résulte des interactions ondes-quai et ondes incidentes-ondes réfléchies, générant un courant associé aux OIS oscillant vers le quai et vers le large. Cette alternance proche du quai est susceptible d'affecter les manœuvres d'accostage. Toutefois, la simulation se limite seulement à des ondes perpendiculaires au quai, sans courant ambiant. Des données *in situ* supplémentaires, notamment sur la vitesse des courants associés aux OIS, permettraient de mieux documenter les conditions réelles au quai et d'imposer certaines contraintes aux simulations. Elles permettraient également d'explorer des scénarios plus réalistes, inspirés d'observations de cette étude, tels qu'un train d'OIS qui frapperait le quai en biais.

Pour mieux appréhender ce phénomène et améliorer notre compréhension de l'accident du *Jaeger Arrow*, nous documenterons la présence et les caractéristiques des OIS aux abords du quai de Grande-Anse. Nous chercherons notamment à quantifier leur nombre, leur amplitude, leur fréquence, leur vitesse, leur direction de propagation ainsi que les courants qui leur sont associés afin d'évaluer leur rôle potentiel dans les conditions ayant conduit à l'accident. Nous déterminerons par ailleurs si leur occurence et leurs propriétés sont reliées aux phases de la marée afin de mieux appréhender certains accostages dans le cas où les vagues sous-marines auraient sur eux un impact significatif.

L'objectif est donc de documenter les OIS aux abords du quai du terminal maritime de Grande-Anse afin de fournir une base pour de futures recommandations sur les protocoles d'approche des navires.

ARTICLE 1

OBSERVATIONS D'ONDES INTERNES NON-LINÉAIRES PRÈS D'UN QUAI ET LEUR POTENTIEL IMPACT SUR LA NAVIGATION

Résumé

Cette recherche est motivée par un incident survenu dans le fjord du Saguenay (QC, Canada) en 2019, où un cargo est entré en collision avec un quai lors de son accostage, entraînant des dommages matériels mineurs tant au navire qu'au quai dans des circonstances mal comprises au moment de l'incident. Notre hypothèse est que des ondes internes solitaires ont pu contribuer au déplacement du navire. Pour tester cette hypothèse, des sondes CTD, des ADCPs, des caméras et un échosondeur ont été déployés durant l'été 2024. Les deux semaines d'échantillonnage ont révélé la présence d'ondes internes solitaires. Ces observations montrent que des trains d'ondes internes ont heurté presque quotidiennement le quai et qu'elles semblent être en phase avec le cycle de marée. Des ondes internes d'une longueur d'onde de 60 m et d'une période de 40 s ont été enregistrées avec des amplitudes pouvant atteindre 10 m et des courants horizontaux associés de l'ordre de 1 $\mathrm{m\,s^{-1}}$. Ces courants semblent suffisamment forts pour affecter la manœuvrabilité d'un cargo lors de l'accostage. Les résultats de cette recherche pourraient contribuer à l'amélioration des simulateurs de navigation, en prenant en compte les effets des ondes internes sur les manœuvres d'accostage.

Observations of non-linear internal waves near a wharf and their potential impact on navigation

1.1 Introduction

Docking maneuvers are complex because pilots must continuously negotiate with environmental forces such as wind, currents, and waves. Yet, we may overlook less known underwater phenomena, which can be either naturally generated or directly induced by cargo ships themselves. While naturally generated internal waves are commonly observed in many stratified regions (Jackson and Apel, 2004), several studies have shown that cargo ships can generate their own internal waves (Watson et al., 1992; Thompson and Jensen, 1993; Grue et al., 2016). As recently suggested by Grégorio et al. (2025), the current of internal waves, may also play a role in docking maneuvers. Indeed, they recently documented an incident that involved the collision of the M/V *Jaeger Arrow* with the wharf of the Grande-Anse Terminal in the Saguenay Fjord. Based on field observations of the sea surface patterns, temperature measurements and idealized numerical simulations, they concluded that the incident was most likely caused by internal waves reflecting off the wharf. They estimated that wave-induced current variations could reach approximately 1 $\mathrm{m\,s^{-1}}$ within 2–3 minutes, which is strong enough to compromise a ship's manoeuvrability. However, this estimate was based on an idealized theory and on numerical simulations that used stratified conditions representative of the Saguenay Fjord. The Saguenay Fjord is also a fjord-like environment where salinity defines the stratification, and where temperature is generally perfectly correlated with salinity, allowing it to be used as a passive tracer, excluding during the winter time (Bourgault et al., 2012). The actual wave-induced currents near the wharf were not directly measured.

In this study, we present new *in situ* and remote observations of non-linear internal waves (NLIWs) near the Grande-Anse terminal to characterize their intensity, recurrence, and potential impact on navigation. Our dataset combines time series from moored instruments, surface imagery from a fixed camera and a drone, as well as transects conducted from a research boat using an echo sounder and a current profiler to document wave trains as they propagate and interact with the wharf. We identify multiple NLIW occurrences and analyze their characteristics to evaluate potential links with tidal phases. A statistical analysis of their timing provides new insights into their recurrence patterns. This work offers practical informations not included in the Grégorio et al. (2025) work that could help port authorities improve safety protocols during docking maneuvers.

1.2 Materials and methods

We conducted two field sampling campaigns near the Grande-Anse terminal (Figure 5): one in fall 2023, and another in summer 2024. All times specified are in UTC.

A CamDo Time Lapse GoPro HERO11 Camera of resolution 5568 × 4872 pixels was installed on the balcony of the administrative building of Port Saguenay (48.40084° N and 70.83633° W) on September 15, 2023, with a clear view of the wharf. This camera captured 1 picture per minute from 10:00 to 23:00 for 3 consecutive weeks until October 5, 2023, and was reinstalled from July 23 to August 14, 2024, capturing 1 picture per minute from 09:00 to 01:00. This setup aims to detect surface signatures of internal waves in the form of dark stripes, as illustrated in Figure 6.

To provide a broader spatial perspective and overcome the constraints of the fixed-angle camera, a drone was also deployed during nearly 30 minutes to 1 hour from the port premises on July 26, 27 and 29 and August 1, 2024 during the passage of NLIW. The images are then georectified using the g_rect Matlab toolbox (Pawlowicz, 2003; Bourgault, 2008; Bourgault et al., 2024). Georectified images ensure that the spatial characteristics of internal waves, such as their position, wavelength, propagation speed, and direction are accurately represented.

A thermometer chain was installed at the western corner of the wharf (48.40178° N and 70.83349° W, red cross in Figure 7) from September 15 to November 1, 2023, and from July

23 to September 11, 2024. The chain was composed of 14 RBRsolo[3] temperature sensors and 1 RBRduet[3] temperature-depth sensor. The temperature-depth sensor was positioned 1 m above the seafloor, followed by 3 temperature sensors spaced 2 m apart. The remaining 11 temperature sensors were positioned 1 m apart. The sensors spanned a total depth of 19 m. Given that the water depth at the wharf is 13.8 m at mean low water, approximately 5 sensors were out of the water during low tides. Each sensor had a sampling frequency of 1 Hz.

The research boat *Colvert*, equipped with a 600 kHz Teledyne RD Instruments Sentinel V 5-beam acoustic Doppler current profiler (ADCP), a 120 kHz BioSonics DT-X echosounder, and a Sea-Bird Electronics SBE-19plus conductivity–temperature–depth (CTD) profiler conducted transects across suspected NLIW trains from July 23 to August 1, 2024 during the daytime. The ADCP and echosounder were towed by the *Colvert* at a depth of about 1.2 m. Hereafter, we refer to the *Colvert*'s ADCP as the towed ADCP. The towed echosounder and ADCP had a bin size of 0.5 m and a sampling period of 1 s.

A 300 kHz and a 600 kHz Teledyne Workhorse Sentinel (WH) ADCP were deployed at the bottom near the wharf (48.40293° N, 70.83286°W and 48.40268° N, 70.83395° W respectively, Figure 7) from July 23 to August 6, 2024. This period covers one neap-spring tidal cycle. The 300 kHz WH ADCP was deployed at a depth of 50 m with a sampling range of 70 m and a bin size of 1 m. Both of the ADCPs have a sampling period of 12 s. Due to unexpected deployment difficulties associated with the steepness of the seafloor, the 600 kHz WH ADCP was installed at 40 m depth instead of the initially planned 30 m. Since it was configured to sample a 30 m range, it did not capture the upper 10 m of the water column, where the pycnocline oscillations induced by internal waves are primarily observed. As a result, data from the 600 kHz instrument were not used in this study, and we refer hereafter to the 300 kHz WH ADCP simply as the moored ADCP.

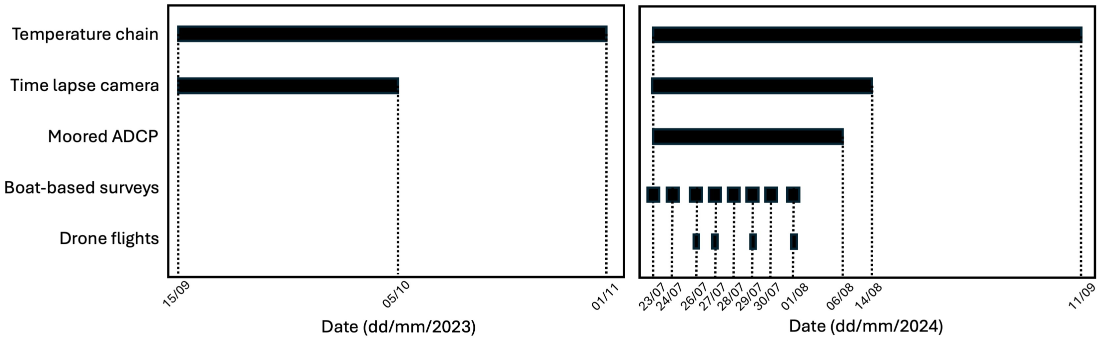

Figure 4 – Gantt diagram of periods which the instruments were operating for 2023 and 2024.

All periods during which the instruments were operating are shown in Figure 4.

In order to analyze how temperature and current signals vary over the dominant semi-diurnal M_2 tidal cycle, a phase-averaging method is applied. This consists in averaging together all data from temperature sensors and moored ADCP measurements that fall within predefined tidal phase intervals. To do so, the semi-diurnal tidal phase $\phi(t)$ of the water level must first be determined for each time point. This phase is then wrapped, meaning it is bounded between $-\pi$ and π. A method described in Richards et al. (2013) computes this phase from the ratio of a signal to its derivative (see their Equation 1). Here, we adopt a slightly different approach based on harmonic analysis. A least-squares fit is first performed to estimate the amplitude h_0 and phase shift ϕ_0 of a pure semi-diurnal M_2 signal that best fits the water-level observations (h), using the form:

$$h(t) = h_0 \sin(\omega_2 t + \phi_0), \tag{1.1}$$

where $\omega_2 = 1.405189 \times 10^{-5}\ \mathrm{rad\,s^{-1}}$ is the angular frequency of the M_2 tide.

Using the trigonometric identity:

$$\sin(\omega_2 t + \phi_0) = \sin(\omega_2 t)\cos(\phi_0) + \cos(\omega_2 t)\sin(\phi_0), \tag{1.2}$$

the signal can be rewritten as a linear combination of sine and cosine functions:

$$h(t) = h_1 \sin(\omega_2 t) + h_2 \cos(\omega_2 t), \tag{1.3}$$

with $h_1 = h_0 \cos(\phi_0)$ and $h_2 = h_0 \sin(\phi_0)$.

From this decomposition, the amplitude h_0 and phase shift ϕ_0 can be recovered as:

$$h_0 = \sqrt{h_1^2 + h_2^2}, \tag{1.4}$$

and

$$\phi_0 = \text{atan2}(h_2, h_1), \tag{1.5}$$

where atan2 is the four-quadrant inverse tangent.

The wrapped phase $\phi(t)$ is then computed as:

$$\phi(t) = \text{atan2}\left[\sin(\omega_2 t + \phi_0), \cos(\omega_2 t + \phi_0)\right], \tag{1.6}$$

which ensures that $\phi(t)$ lies within $[-\pi, \pi]$.

The full tidal cycle is then divided into phase bins of width:

$$\Delta\phi = \frac{2\pi}{50} = 0.1257, \tag{1.7}$$

corresponding to approximately 14.90 minutes for an M_2 period of 12.42 hours. This choice of dividing the signal into 50 bins, which corresponds to roughly 15 minutes, provides a sufficient temporal resolution to evaluate the timescale relevant to large ship maneuvering. Data points are grouped according to their tidal phase, and averaging is performed within each bin to analyze the variable of interest as a function of tidal phase.

A central question of this research is to determine the impact of surface currents induced by NLIWs on ship manoeuvrability. While a general answer would be desirable, the effect is ship-specific because vessels differ in draught and because surface currents in such a stratified, fjord-like environment are strongly vertically sheared. For this reason, a standard definition of "surface currents" must be established. In this study, "surface currents" refer to the current averaged over the upper 13 m of the water column. This depth was chosen based on the information that the Port of Saguenay guarantees a minimum water depth of 13.8 m at low mean tide at the Grande-Anse wharf. We therefore consider 13 m to be close to the maximum draught of a ship docking at this terminal. It should thus be kept in mind that the results presented here may not directly apply to vessels with a substantially smaller draught.

Velocity data from the moored ADCP were first cleaned to remove all non-natural events associated with the presence of cargo ships near the wharf. Cargo ships are known to generate internal waves or perturbations (Watson et al., 1992; Thompson and Jensen, 1993; Grue et al., 2016; Grégorio et al., 2025) that could bias statistics. These events were identified using the camera and the moored ADCP's echosounder and the corresponding data were replaced with NaN values. All remaining data reaching unrealistic velocities (around 10 $\mathrm{m\,s^{-1}}$) were also removed manually. The moored ADCP side-lobe, corresponding to 6% of the total depth below the surface (Lentz et al., 2022), was also replaced with NaNs to avoid any additional contamination. Excluding the data removed because of side-lobe contamination, the remaining removed data constitute a negligible fraction of the dataset (less than 1%).

The water height, recorded by the moored ADCP's depth sensor, was filtered using a low-pass Butterworth filter with a cutoff frequency of 1/(1800 s) to remove high-frequency instrumental noise from the general instability of *in situ* measurements over short timescales. For unknown reasons, the total depth measured by the pressure sensor was offset by approximately 5 m compared to the sea surface position inferred from the strong acoustic backscatter, and was thus corrected to match that reference.

After the cleaning, the kinetic energy density K, in $\mathrm{J\,m^{-3}}$, was computed at each depth as follows:

$$K(z,t) = \frac{\rho_0}{2}(u^2 + v^2 + w^2) \tag{1.8}$$

where ρ_0 is the freshwater density, taken as 1000 $\mathrm{kg\,m^{-3}}$, and u, v and w are the East-North-Up (ENU) velocity components in $\mathrm{m\,s^{-1}}$, respectively. We then averaged K over the surface thickness ΔH, as:

$$\overline{K}(t) = \frac{1}{N}\sum_{k=1}^{N} K_i(z_k, t), \tag{1.9}$$

where K_i is the kinetic energy interpolated on a regular vertical grid with spacing $\Delta z = 0.5$ m, extending from the surface down to 13 m and $N = dH/dz$ is the number of interpolated grid points. Note that the subscript i is not an index. Once $\overline{K_i}(t)$ was computed, the signal was filtered using a 4^{th}-order Butterworth band-pass filter with cutoff frequencies of 1/(30 s) and 1/(360 s). This frequency band, intended to encompass the typical periods of internal solitary waves in the area, 120 s (Grégorio et al., 2025), was chosen based on visual inspection of several representative cases. Prior to filtering, NaN values were temporarily filled using linear interpolation of the surrounding data to provide the filter with a continuous time series. The NaNs were then reinserted into the filtered signal. This process yielded the perturbation kinetic energy time series, denoted $\overline{K_i}'(t)$. The variable $\overline{K_i}'(t)$ is then squared, phase-averaged and square-rooted to produce the standard deviation, that is:

$$\sigma\left(\overline{K_i}'\right) = \sqrt{\left\langle \left(\overline{K_i}'\right)^2 \right\rangle}. \tag{1.10}$$

A procedure similar to that used for kinetic energy was applied to the temperature data to isolate the internal wave signal. The water height, recorded by the temperature-depth sensor, was first filtered with a 4^{th}-order Butterworth low-pass filter with cuttoff frequency of 1/(1800 s) to remove all the high-frequency instrumental noise. Temperature data were then interpolated onto a regular vertical grid with spacing $\Delta z = 0.5$ m, extending from the surface down to a depth of $\Delta H = 13$ m. For each interpolated depth z_k, the temperature time series was filtered using a 4^{th}-order Butterworth band-pass filter with cutoff frequencies of 1/(30 s) and 1/(360 s). This yields the perturbation temperature field $T_i'(t, z_k)$. The resulting $T_i'(t, z_k)$ is then squared and averaged over the depth ΔH, as follows:

$$\overline{(T_i')^2}(t) = \frac{1}{N} \sum_{k=1}^{N} \left(T_i'(t, z_k)\right)^2 . \tag{1.11}$$

We applied phase-averaging to $\overline{(T_i')^2}(t)$ to get $\left\langle \overline{(T_i')^2} \right\rangle$, from which the square root was taken to yield the phase-averaged standard deviation of the perturbation temperature:

$$\sigma\left(\overline{T_i'}\right) = \sqrt{\left\langle \overline{(T_i')^2} \right\rangle}. \tag{1.12}$$

To perform these statistics and generate the observational figures, we use the same temporal resolution as the sampling period of the instruments. This also ensures that short frequency phenomena are preserved.

1.3 Results

Consistent with the preliminary observations reported by Grégorio et al. (2025), the new data support the view that the area off the Grande-Anse terminal is regularly affected by NLIWs, but, at this stage, we had no information on how many NLIW reached the wharf. It is important to note that we therefore consider each NLIW train as an *event*. Here, a total of 48 events of internal waves train were identified, 23 in fall 2023 and 25 in summer 2024, based on visual interpretation of sea surface patterns captured by the camera. However, the camera can only detect the presence of NLIW during daytime and under calm weather conditions, and therefore provides only a partial account of the internal wave field in the area. The thermometer chain, capable of detecting oscillation patterns even during nighttime and adverse weather conditions, recorded 74 events in 2023 and 101 in 2024 as determined by visual inspection of the time series. Examples of such events recorded by the temperature data will be presented below. Taking together the results of the two independent analyses, the events occurred on average 1 hour 57 minutes after high tide, with the timing ranging from 1 hour 20 minutes to 2 hours 50 minutes after high tide. The camera's images indicate mainly events who are coming from the upstream of the fjord. Since temperature oscillations do not always provide unambiguous evidence of NLIW, the precise number of events detected by the thermometers can remain uncertain with a margin of error of ten events. In the following, we present the event of July 24, 2024 (Event 1), given the clarity and quality of the observations collected on that day.

The Figure 6 image shows the clearest surface signature of NLIWs that we obtained during the two field campaigns. Dark and light streaks can be seen propagating toward the wharf and downstream. The number of streaks suggests the presence of 8 NLIWs. The clarity of this surface signature was enhanced by the weather conditions and the nearly full sunlight that day. The following event in Figure 7 also displays very distinct surface signatures, but the different weather conditions reduced the contrast between the streaks.

Figure 7 shows the characteristic surface signature of an NLIW train, showing alternating dark and light streaks propagating downstream toward the wharf. The first wave of the train propagated at approximately 0.8 $\mathrm{m\,s^{-1}}$, based on the time elapsed between 11:46:31 and 11:56:30. The two grey markers on the 11:46:31 and 11:56:30 images indicate the distance used to estimate the propagation speed. By 11:48:31, part of the incident wave field near the wharf appears to have already reflected off the nearby shoreline. The wave crests extend almost across the entire fjord, with 11 incoming NLIWs clearly visible at 11:56:30. At the same time, 2 reflected waves can also be distinguished, propagating seaward across the incoming wave train.

The *Colvert* also crossed this wavetrain multiple times measuring the magnitude and the direction of the NLIW' associated currents. The different segments of the *Colvert*'s track are represented in Figure 5. As shown in Figure 7 and Figure 5, the *Colvert* initially sampled the incident waves, followed by an attempt to capture the reflected waves. The towed ADCP and echosounder data for the reflected wave trains are not presented here, as the measurements does not allow a clear distinction of those waves. Indeed, the interaction between reflected and incident waves that did not reach the wharf likely contributes to uncertainty in estimating the true magnitude of the reflected waves.

Current data from both the towed and moored ADCPs, initially collected in the ENU reference frame, were rotated such that one component of the horizontal currents was rotated to visually aligned with the direction of wave propagation (30° clockwise, relative to the east component for Event 1). The along-wave current associated with the incident waves reached about 0.5 $\mathrm{m\,s^{-1}}$. The wavetrain reached the dock at 11:50:00 (Figure 9, bottom panel), roughly 2 hours after high water (9:50). The echogram in Figure 8 suggests that the pycnocline was located at a depth of approximately 3 m, within the wavetrain evolved. Across the wavetrain, maximum amplitudes were around 3 m, with wavelengths on the order of 30 m.

While the towed ADCP echogram (Figure 8) indicates a 3 m amplitude, the temperature measurements (Figure 9) show a 6 m oscillation impacting the wharf, about twice the initial pycnocline depth, consistent with wave reflection. This observation is also consistent with Grégorio et al. (2025) where similar proportions were computed. The moored ADCP, similarly to the towed ADCP, records a maximum current velocity of 0.5 $\mathrm{m\,s^{-1}}$ for this wave train, followed by what could be identified as a front (from 12:05), exhibiting comparable velocities. The echogram captured by the moored ADCP shows a similar evolution into a front. All fronts in this study were identified visually.

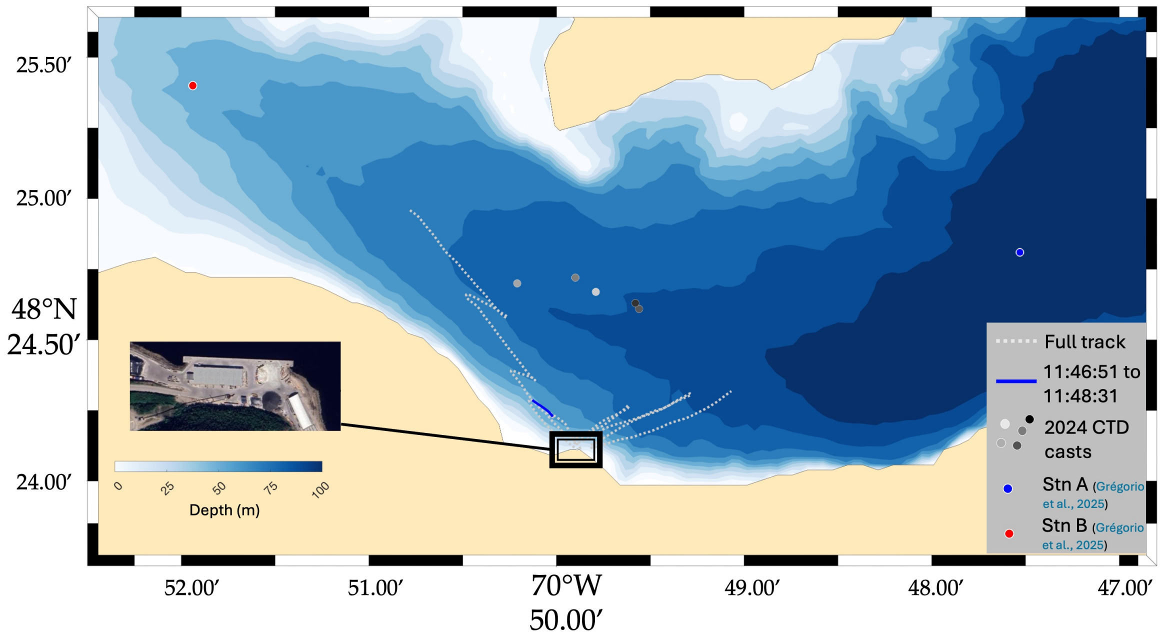

Figure 5 – Map of the Upper Saguenay Fjord centered on the Grande-Anse Terminal of Port Saguenay. The black double-line box indicates the location of the terminal, shown in the inset as a satellite image (source: Google Earth). The grey dashed line represents the full trajectory of the *Colvert* on July 24, 2024, during Event 1, while the solid blue segment highlights a portion of the same transect corresponding to the data shown in Figure 8. The dots indicate the locations where CTD profiles were collected, including the 2024 casts and Stations A and B from Grégorio et al. (2025), all of which are presented in Figure 16. There are no significant underwater reliefs, which rules out the possibility of internal tides.

Figure 6 – Camera image of the Figure 14 and of the bottom right SAR image in Figure 15 (Event 4) on August 5, 2024 at 22:28:31. We observe a wavetrain propagating downstream and impacting the studied wharf. This is one of the clearest surface signatures obtained during the Fall 2023 and Summer 2024 campaigns.

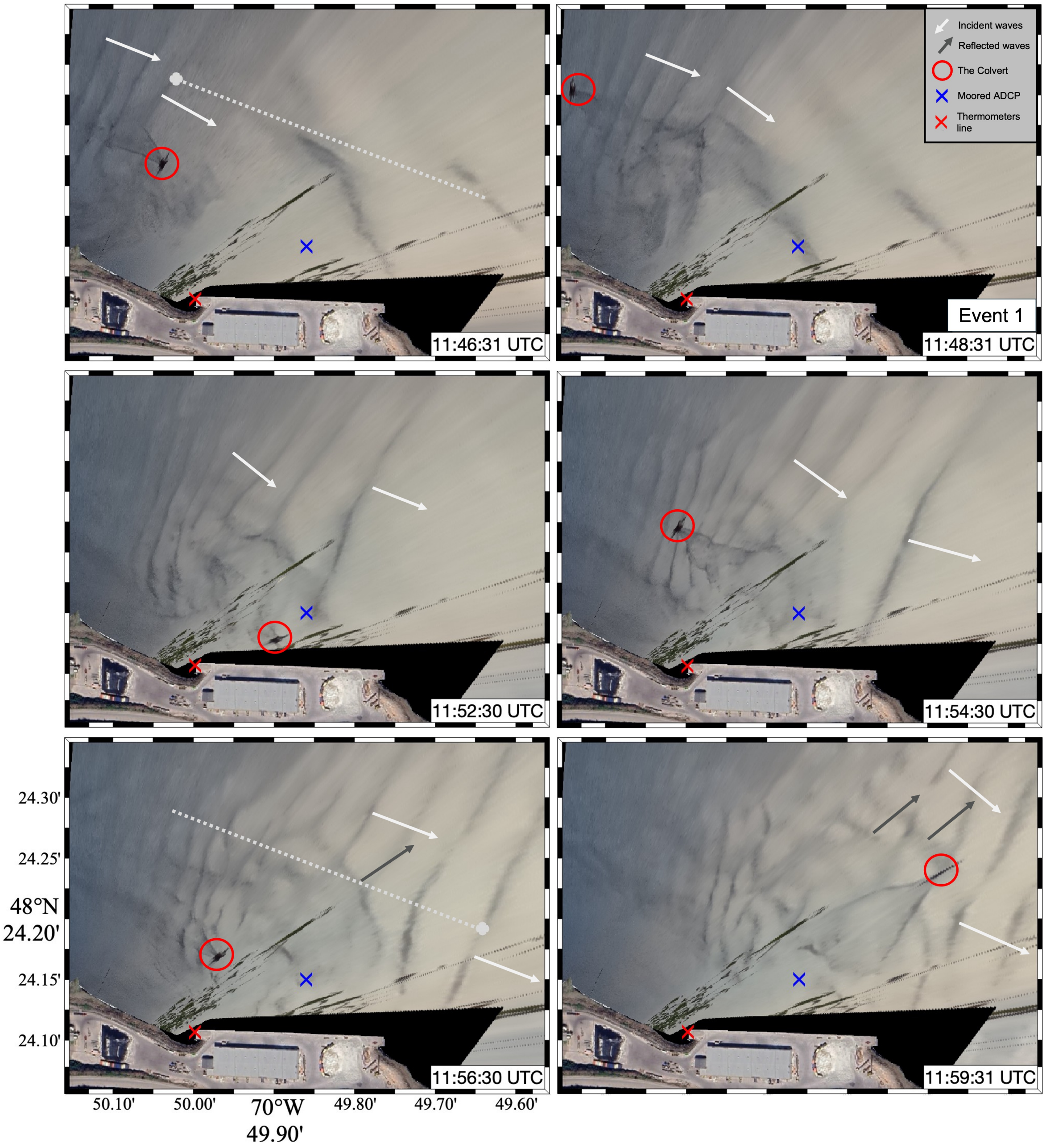

Figure 7 – Sequence of georectified images showing the sea surface signature of internal waves interacting with the wharf at Grande-Anse during Event 1. Images were taken on July 24, 2024. The red cross marks the position of the thermistor chain, while the blue cross indicates the position of the moored ADCP. Wave propagation direction, illustrated by arrows, was inferred from the sequence of consecutive images. The star denotes the position of the research boat *Colvert*. The grey dashed line indicates both the distance and orientation of the axis along which the wave's propagation speed was calculated.

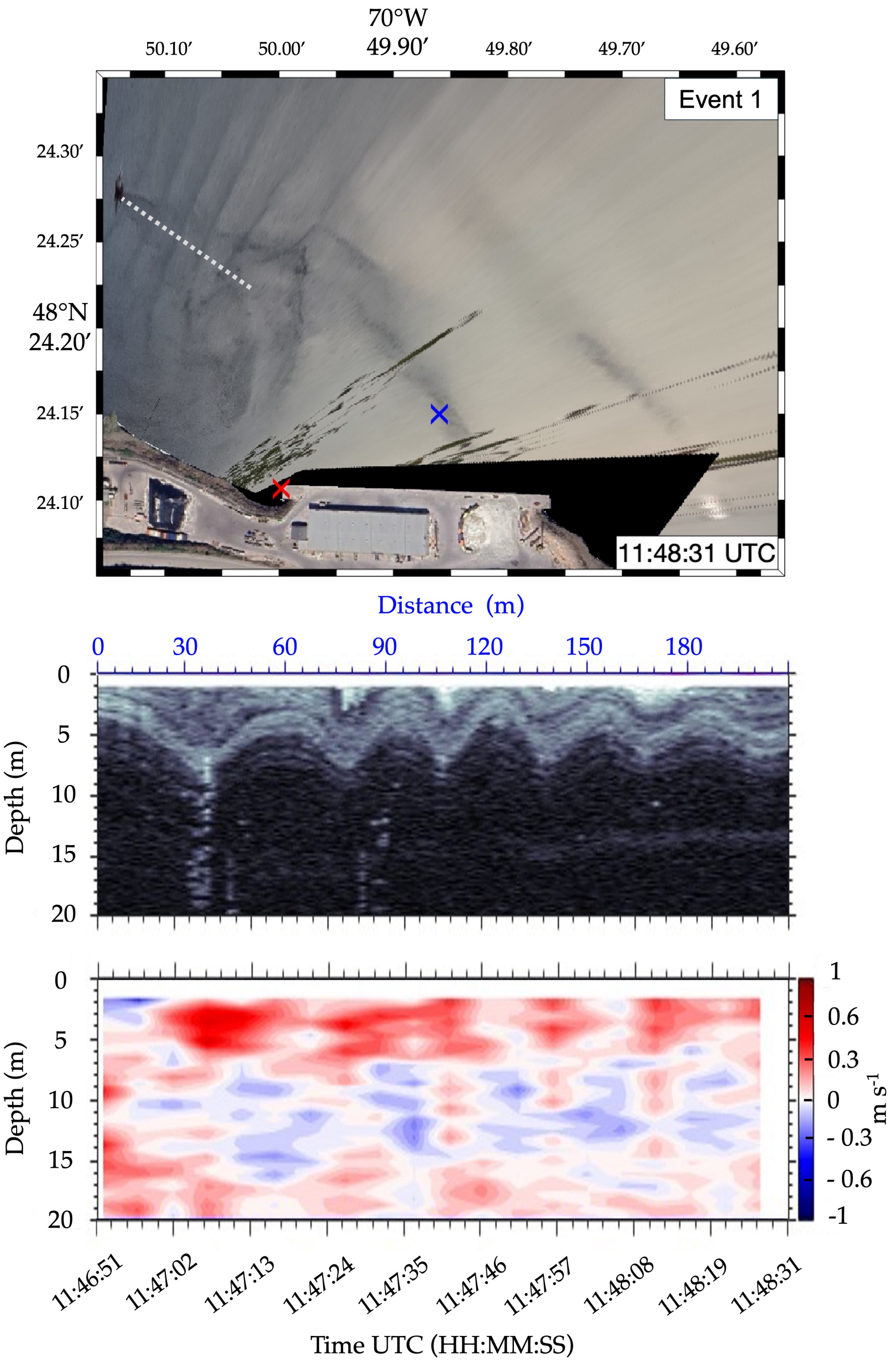

Figure 8 – Top panel: georectified image taken at 11:48:31 on July 24, 2024, corresponding to the top-right frame of Figure 7. The grey dashed line is the portion of the transect corresponding to the blue segment in Figure 5. Middle panel: echogram recorded by the towed ADCP. Bottom panel: horizontal along-wave current component measured by the towed ADCP.

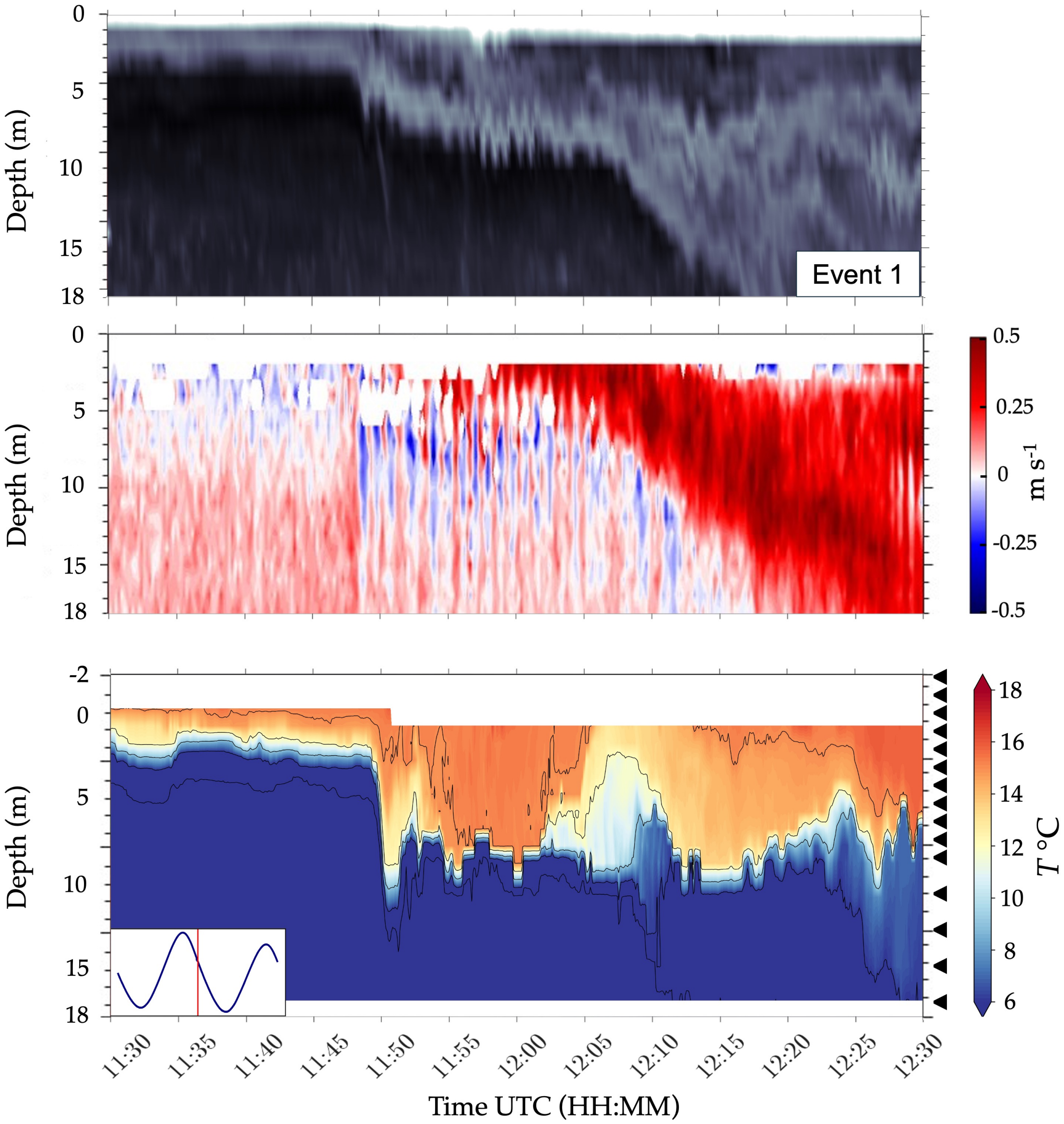

Figure 9 – Top panel: echogram recorded by the moored ADCP (blue cross in Figure 7). Middle panel: horizontal alongwave current component measured by the moored ADCP. Bottom panel: Hovmöller diagram of temperature at the wharf. Each black triangle on the right indicates the depth of a thermometer. The tidal cycle for this event is shown in the bottom left-corner. All panels correspond to Event 1 on July 24, 2024.

On July 26, 2024, a similar train of NLIWs was sampled by the *Colvert* between 2 and 3 hours after high water, but farther downstream (Event 2, Figure 10). As for Event 1, the ENU current data were rotated to visually align with the wave propagation direction (25° counter-clockwise relative to the east component for Event 2). The waves reached amplitudes approaching 10 m and were associated with stronger horizontal currents than in Event 1, locally reaching 1 $\mathrm{m\,s^{-1}}$ (Figure 10). Opposing flows of similar magnitude produced velocity differences of up to 2 $\mathrm{m\,s^{-1}}$ between the wave crests and troughs. The wavetrain remained well defined as it propagated downstream, eventually colliding with the fjord's side. As in Event 1, the NLIW signature extended across nearly the entire width of the fjord.

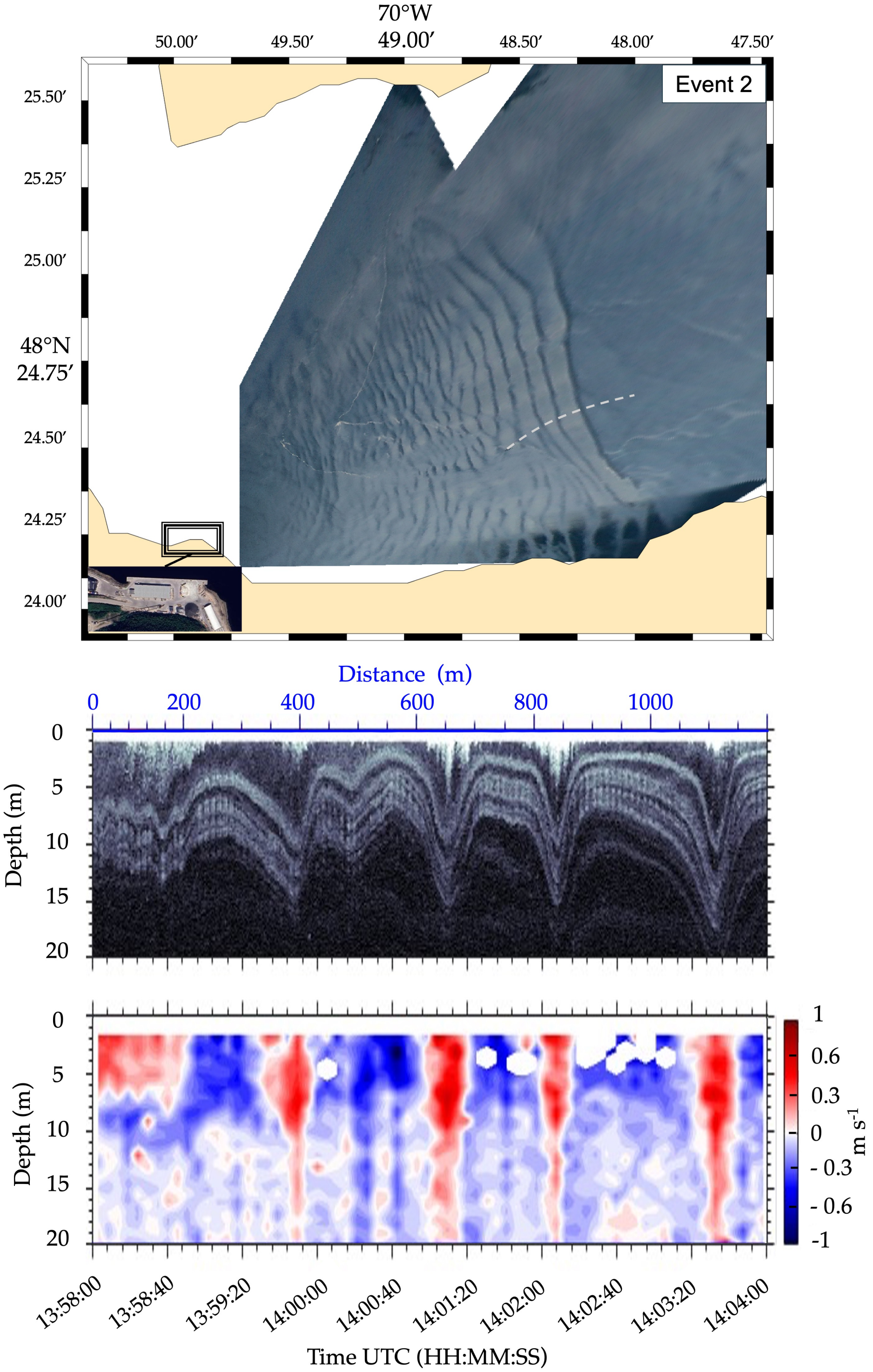

Figure 10 – Top image: georectified drone's picture of the NLIWs train measured for the Event 2 at 13:59 on July 26, 2024. The dashed grey line represents the transect of the *Colvert* shown in the middle panel for the echogram and in the bottom panel for the horizontal currents measured by the towed ADCP.

The camera, the thermometer chain and the moored ADCP, have sampled several other events shown in Figure 11 to Figure 14. In 2023, the NLIWs were located farther away from the wharf (Figure 11). This explains why the georectified images encompasse a larger area next to the wharf than for the August 2024 events (Figure 7, Figure 8, Figure 13 and Figure 14). The image quality is also lower than for the 2024 events, because covering a larger area requires stretching the image further, which increases distortion at its spatial limits, a typical characteristic of georectified images. All presented events occur 1.5 to 2 hours after high tide and originate from upstream, like Event 1 (Figure 7) and Event 2 (Figure 10). We hereafter refer to the NLIWs who occur 1.2 to 2.8 hours after the high tide and originate from upstream as *Chicou* waves named after the city of Chicoutimi, upstream of the study area. This term is only intended to make the description of the events clearer.

We can observe the surface signatures of the *Chicou* waves in 2023 (Figure 11). They propagate downstream and do not appear to reach the wharf. Nonetheless, a reflection was observed on September 30, 2023, against the nearby shoreline (Figure 11). Moreover, the surface signature seems to be associated with disturbances in the thermometer chain lasting from 1 to 4 hours (Figure 12), which are not always clearly identifiable as regular oscillations. It is important to note that stratification progressively weakened over the course of fall 2023. On September 15, 2023, the surface temperature was approximately 18 °C, while temperatures below the pycnocline remained below 6 °C. By September 30, the surface had cooled to about 13 °C, with temperatures below the pycnocline around 6 °C. Despite this change in stratification, clear oscillations were observed on both September 15 and September 28, 2023.

In summer 2024, Figure 7, Figure 8, Figure 10, Figure 13, and Figure 14 show much clearer surface signatures than in fall 2023. Contrary to 2023, the *Chicou* waves appear closer and reach the wharf, with the previously described reflection against the wharf in Event 1 (Figure 7). The oscillations sampled along the thermometer chain are consistent with Grégorio et al. (2025), where the first oscillation is the largest. This characteristic is evident in both Event 1 (Figure 9), Event 3 (Figure 13), and Event 4 (Figure 14). The summer 2024 stratification remains well defined, unlike the weaker stratification of fall 2023, with surface temperatures around 18 °C and temperatures below the pycnocline remaining below 6 °C. For Event 3 and Event 4, current data were rotated to visually align with the wave propagation direction (30° clockwise relative to the east component for Event 3 and Event 4). In 2024, Figure 13 shows currents reaching up to 0.5 $\mathrm{m\,s^{-1}}$, with the echogram revealing oscillations approaching 5 m. Notably, Event 4 observations indicate that a pronounced surface signature does not necessarily correspond to large currents or amplitudes (Figure 14).

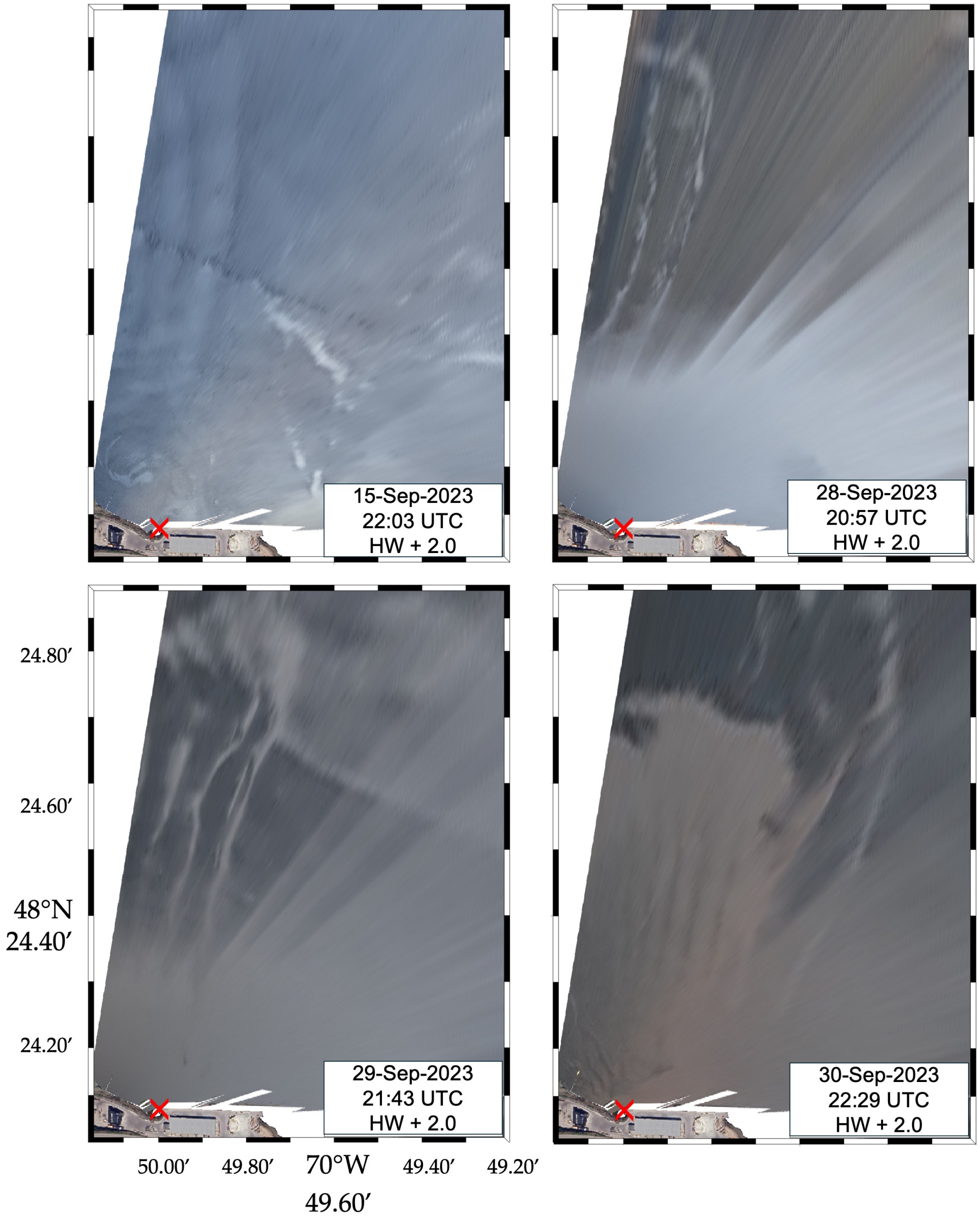

Figure 11 – Georectified pictures of *Chicou* waves from September 2023. The number of hours after the high water (HW) is indicated in the bottom-right corner of each picture.

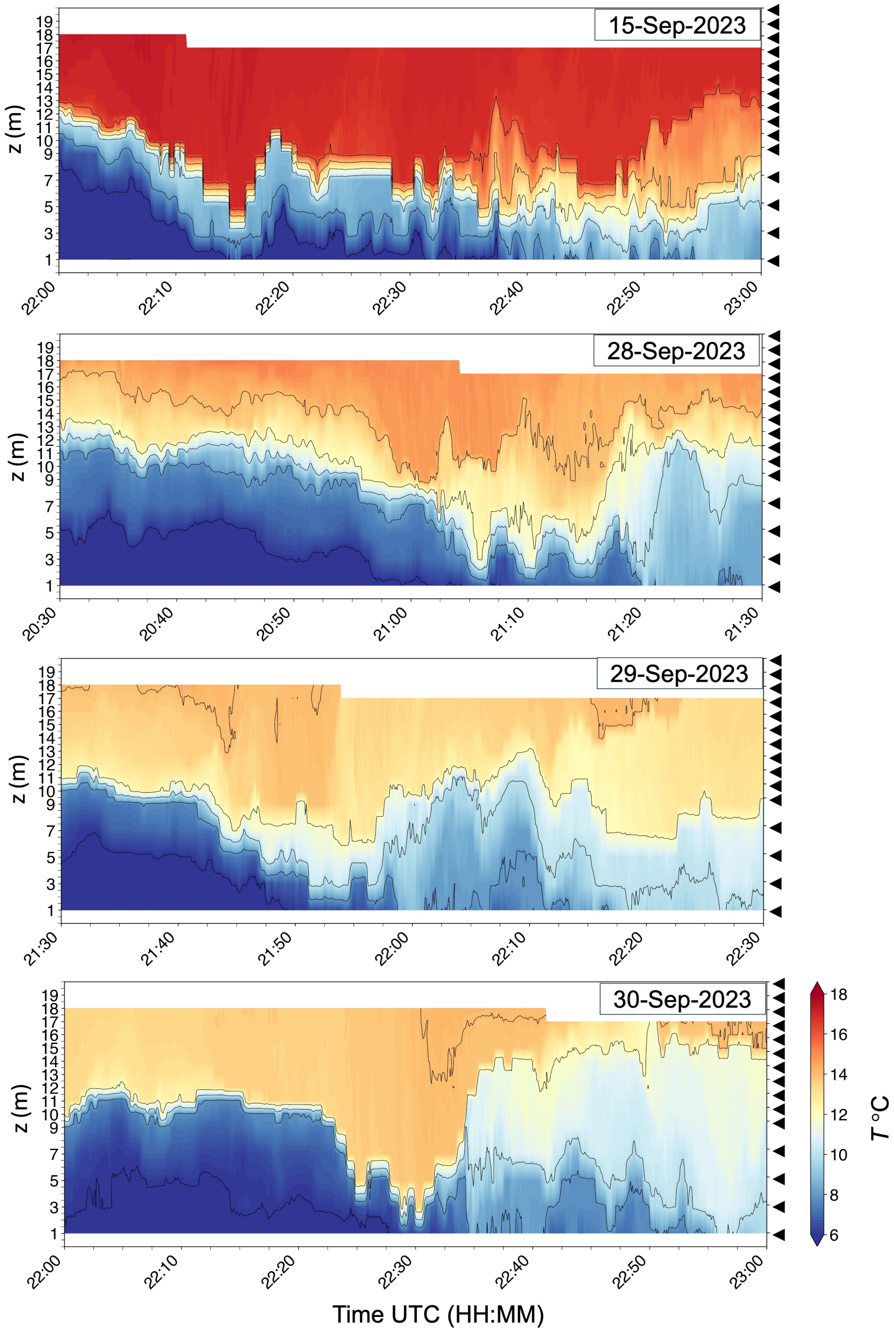

Figure 12 – Temperature fields corresponding to the same events as in Figure 11. The September 15 event shows the strongest stratification, but not necessarily the clearest oscillations compared to September 28 at 21:10.

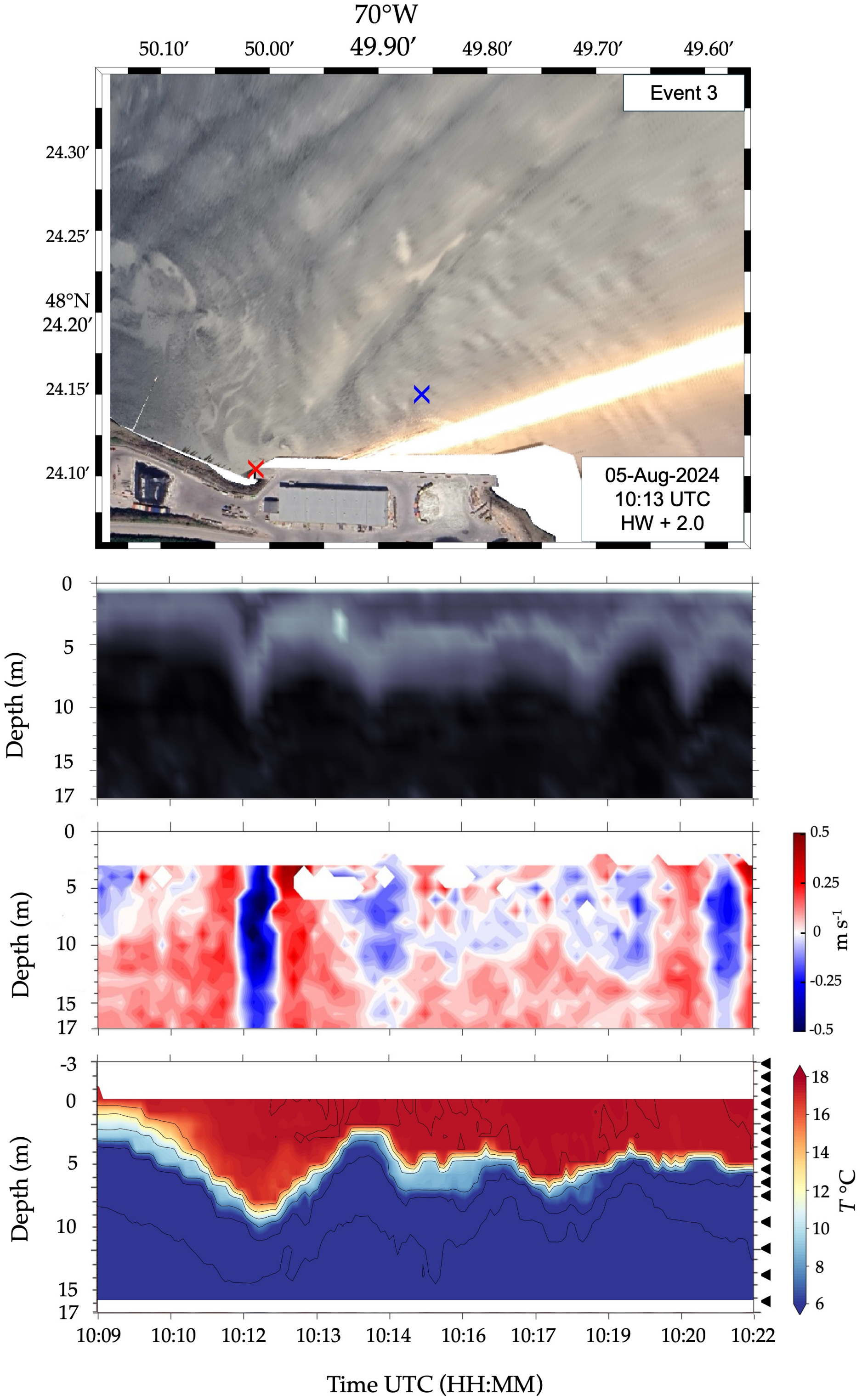

Figure 13 – Top image: georectified picture of Event 3 on August 5, 2024 at 10:13. First panel: associated moored ADCP echogram. Second panel: associated horizontal currents. Third panel: associated temperature field.

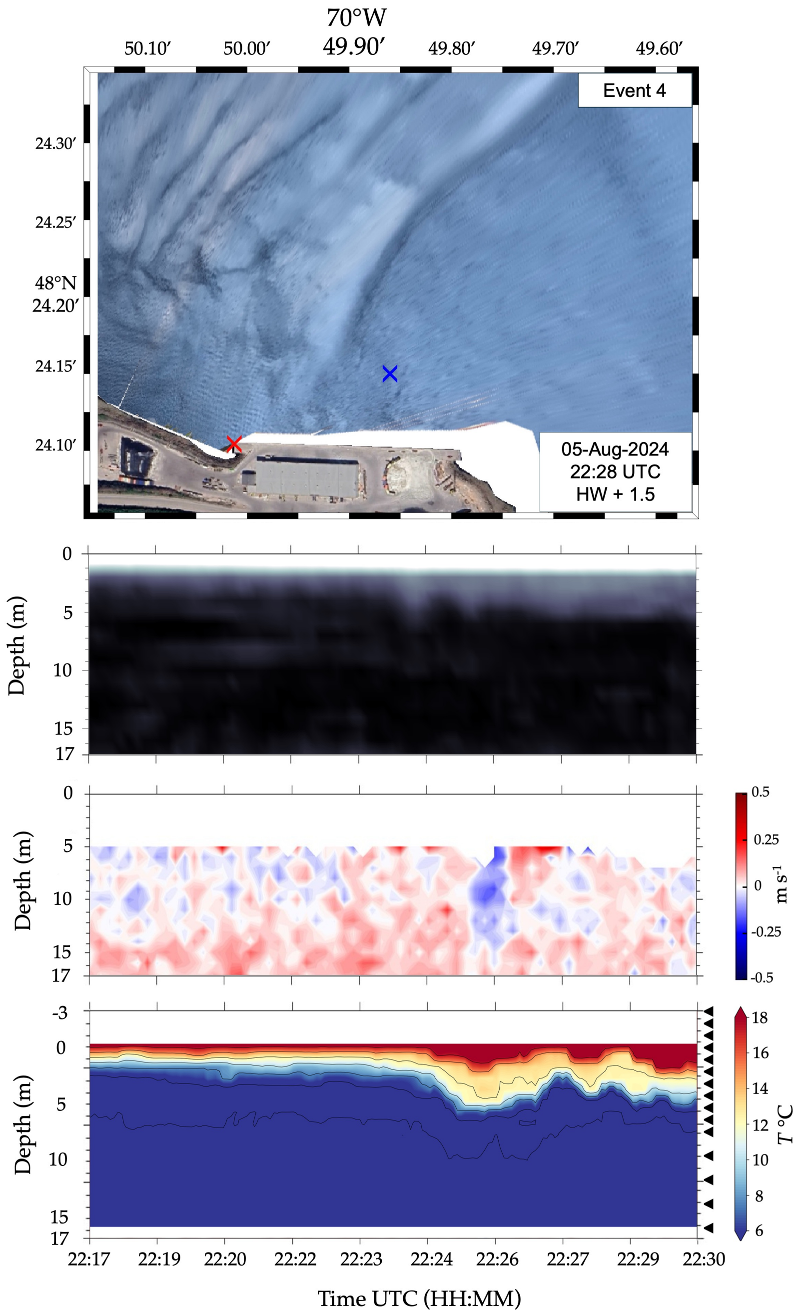

Figure 14 – Top to bottom: georectified image of Event 4 on August 5, 2024 at 22:28; associated echogram; associated horizontal currents associated temperature field.

The *Chicou* waves are not limited to 2023 and 2024. We examined all available SAR (synthetic aperture radar) images since 2016 in search of further evidence for NLIWs in the area. A total of 20 events were identified, 9 of which are presented here, occurring 1.5 to 2.5 hours after high tide (Figure 15). These images complement our observations, showing similar crest orientation and width as seen during Events 1 to 4 (Figure 7, Figure 8, Figure 10, Figure 13 and Figure 14). In addition to these supplementary data, we were fortunate to capture a SAR image of Event 4 (bottom right picture), providing a rare coincidence of *in situ* measurements (Figure 6 and Figure 14) and a satellite observation.

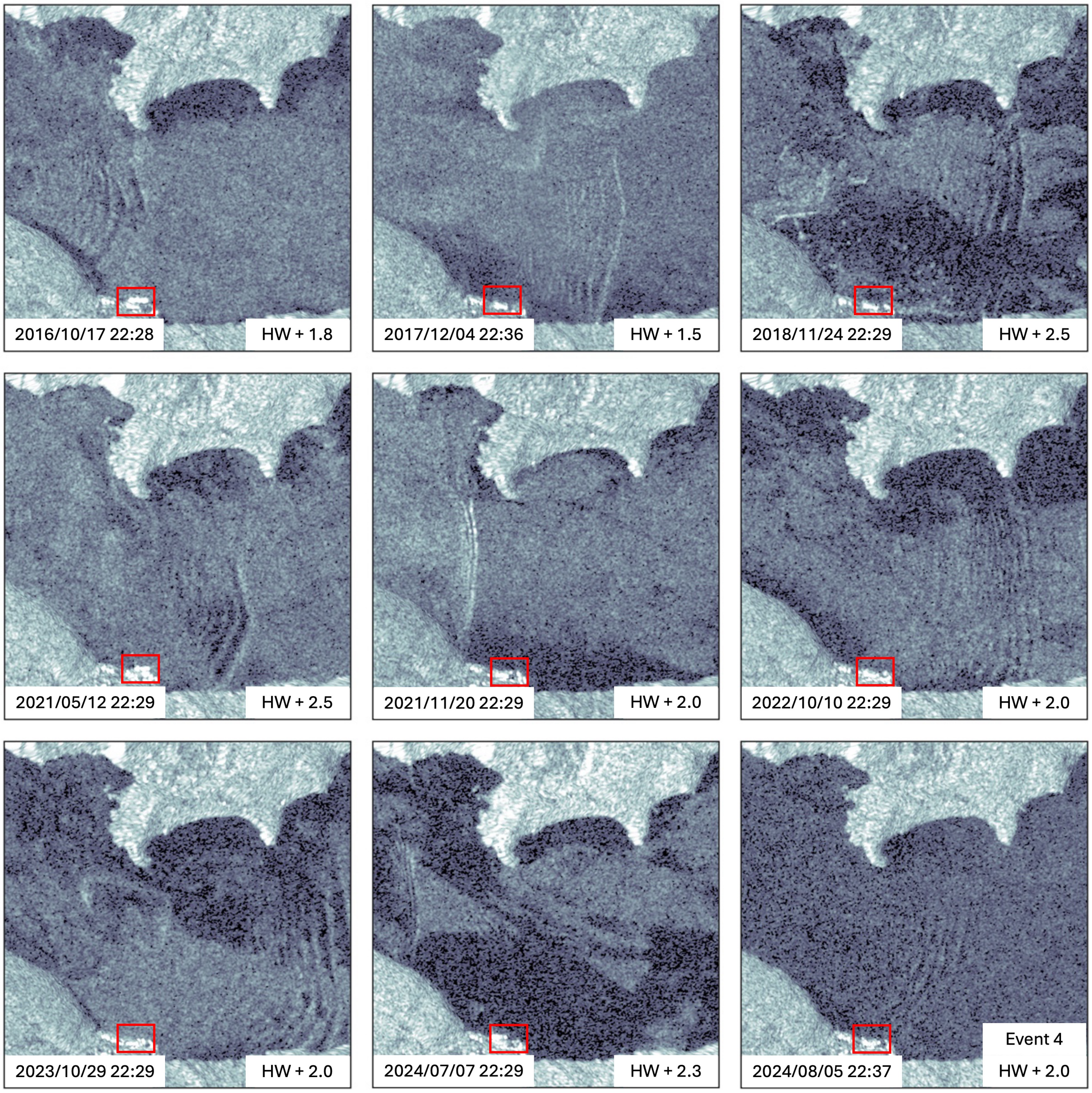

Figure 15 – A selection of 9 out of 20 SAR images identified showing the surface signatures of internal wavetrains off the Grande-Anse Terminal (red box). The date and time stamp in the lower left corner of each image represents the sensing time and in the lower right corner there is the number of hours after the closest HW on that day. The internal waves always appear in the region roughly between 1.5 and 2.5 hours after the time of local high water. (Image source: Copernicus Sentinel-1 data).

It is also interesting to consider whether these events are influenced by changes in stratification. During the 2024 *Colvert* campaign, samplings spanned an entire neap-spring tidal cycle: the survey began near spring tide on July 23 and extended toward neap tide by July 30. Because the generation of NLIWs is closely linked to stratification, CTD casts were performed almost daily at mid-fjord in front of the wharf (Figure 16). The water column exhibited some variability, but the observed density changes could not be explained by the tidal cycle or by the neap-spring cycle, as they did not follow any systematic or repeatable pattern. The pycnocline persistently located around 5 m depth, consistent with the structure reported at Station B (Grégorio et al., 2025).

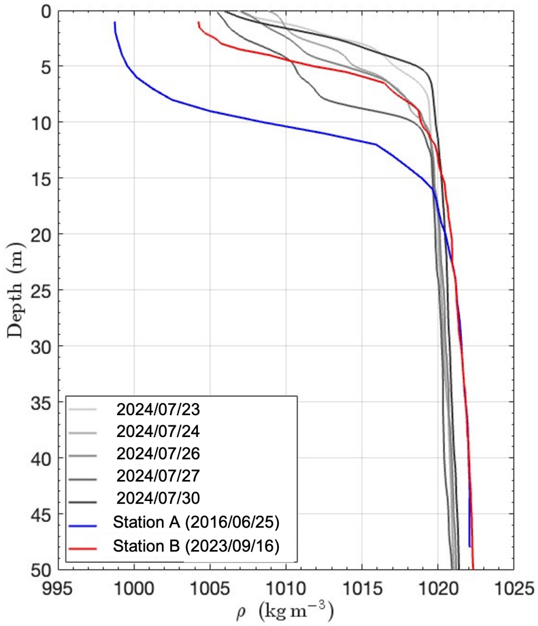

Figure 16 – CTD casts sampled during the summer 2024 mission are shown in grey. Stations A and B, as reported in Grégorio et al. (2025), are shown in green and blue, respectively. The locations of the casts are shown in Figure 5 with their corresponding colors.

Another question is whether the *Chicou* waves or other events appear at a particular phase of the semi-diurnal tidal cycle. Assuming that NLIWs generate bursts in $\overline{K}'$ and $\overline{(T')^2}$, we superimposed these two indicators onto the tidal cycle for early August (Figure 17). Distinct bursts seem to systematically appear at the beginning of each ebb tide. This is quantitatively confirmed by computing the phase-averaged of $\overline{K}'$ and $\overline{(T')^2}$ over the summer of 2024 (Figure 18). The result of this statistical analysis shows that enhanced activity occurs between 2 and 4 hours after high tide, in agreement with the expected timing of the *Chicou* waves. In contrast, no such bursts were observed during fall 2023, which could explain in part by the weaker and less defined events shown in Figure 11 and Figure 12. To test the sensitivity of the results to the choice of 13 m, we selected 13, 11, 9, and 7 m to assess how this affects the results. The values of temperature and kinetic energy are affected, but not the timing.

The camera observations support this contrast: of the 23 events recorded in 2023, 12 were identified as *Chicou* waves (52%), whereas in 2024, 21 out of 25 events (80%) were identified as such. Similar proportions were obtained from the thermometer chain data, with 41 *Chicou* waves out of 74 events (55%) in 2023, and 72 out of 101 (71%) in 2024. It should be noted that, to identify an event as a *Chicou* wave based on the thermometer chain data, only the timing relative to high tide was considered.

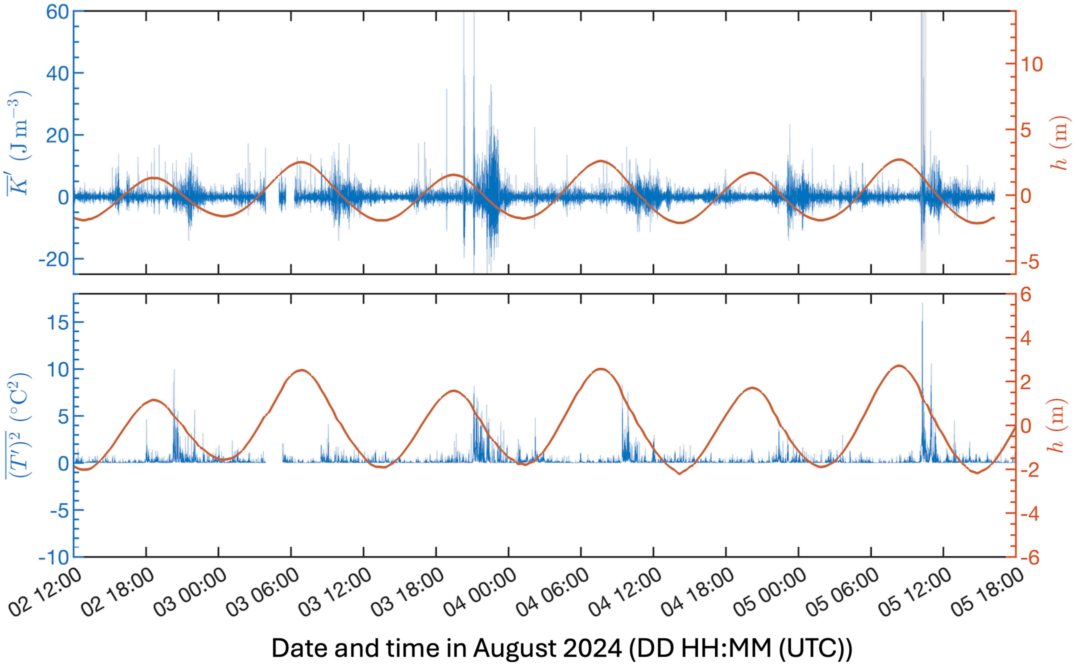

Figure 17 – Top panel: Depth-averaged filtered kinetic energy ($\overline{K}'$) in August 2024 (blue) compared to the sea surface height (orange). Bottom panel: Depth-averaged filtered temperature variance ($\overline{(T')^2}$) in August 2024 (blue) compared to the sea surface height (orange). On both panels bursts are constantly observed after the high tide.

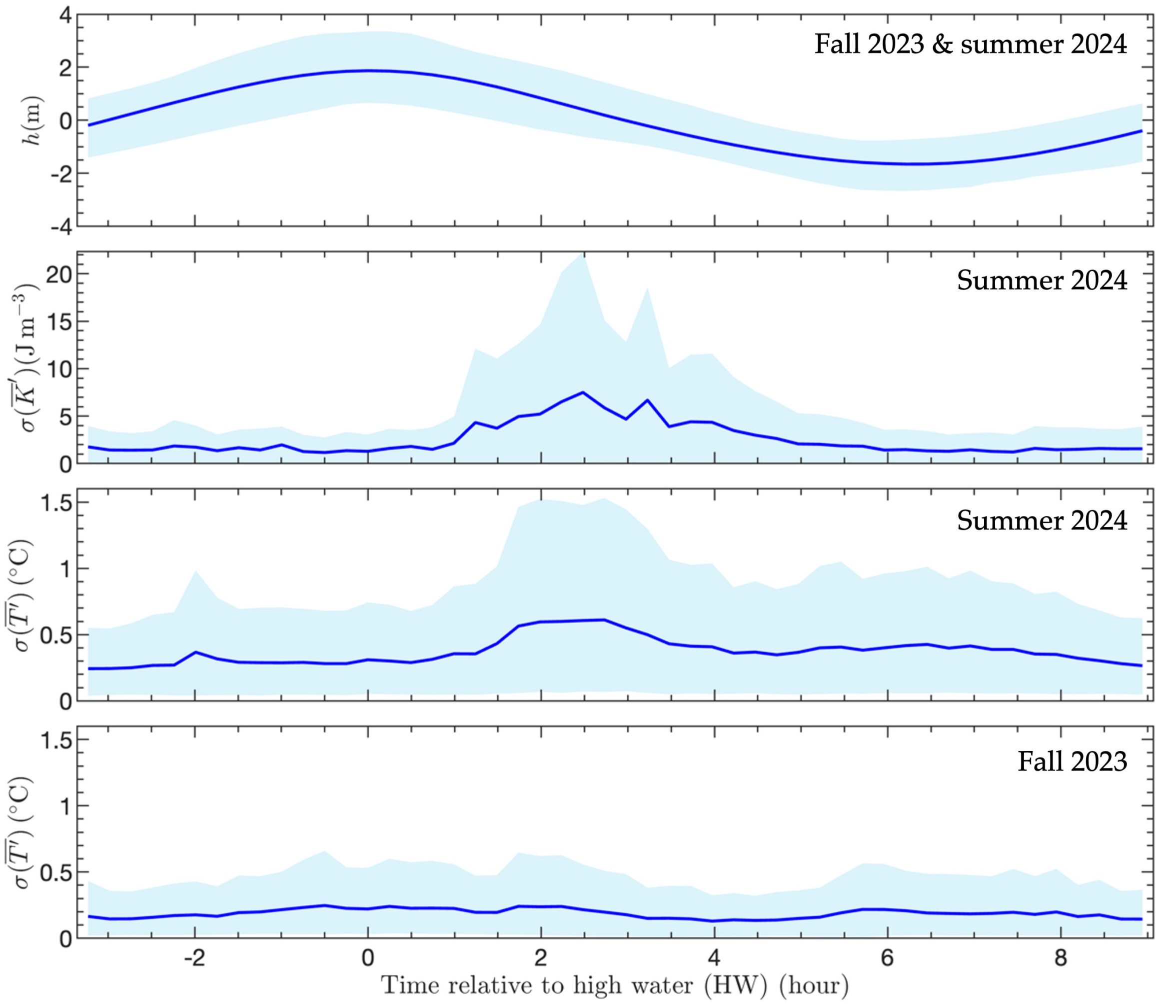

Figure 18 – First panel: Phase-averaged sea surface height (h) for fall 2023 and summer 2024. Second panel: Phase-averaged filtered kinetic energy standard deviation ($\sigma(\overline{K}')$) for summer 2024. Third panel: Phase-averaged filtered temperature standard deviation ($\sigma(\overline{(T')})$) for summer 2024. Fourth panel: Same as the third panel but for fall 2023. In all panels, the 97.5% confidence interval is shown in light blue.

1.4 Discussion

We presented several observational evidences of the presence of NLIWs near the wharf. The repeated presence of *Chicou* waves during the campaigns and the SAR images highlights how this phenomenon is recurrent in this area. The *Chicou* waves arrive at a consistent time relative to the tide and appear to reach the Grande-Anse wharf, reflecting off it or the adjacent shoreline (Figure 7 and September 30 event in Figure 11). These reflections are difficult to quantify in the towed ADCP and echosounder data, as the incident waves propagate across them. Here, the direction of incident and reflected waves differs from the directions of the waves reported by Grégorio et al. (2025), which reflected waves were oriented opposite to the incident ones.

Grégorio et al. (2025) also showed, using an idealized simulation for this region, that the first oscillation of the NLIWs at the wharf is roughly twice as large as the incoming waves for NLIWs of the same amplitude. This result is consistent with the temperature field shown in Figure 9. The first large oscillation observed by the temperature chain for Event 1 (Figure 9) is likely the result of a superposition of incoming waves against the wharf and not an onlywave, shortly after the impact against the wharf at 11:50. One might expect that the associated currents could intensify with this larger oscillation (Osborne and Burch (1980)). However, at the wharf, the incident and reflected currents cancel each other, so no additional risk should be expected despite the increased oscillation (Grégorio et al., 2025). A closer moored ADCP to the wharf in the future may help to confirm this hypothesis.

It is important to note that the 2023 *Chicou* waves in Figure 12 are less clearly defined than the 2024 *Chicou* waves (Figures 9–10 and 13–14) in the temperature data. Indeed, the temperature data perturbations in 2023 do not always display regular oscillations but instead often resemble the passage of a front. It would have been valuable to confirm whether these possible 2023 fronts involved significant horizontal currents, as observed in Event 1 (Figure 9). As mentioned before, a moored ADCP closer to the wharf may help to measure the possible currents linked to this phenomenon.

Our statistical analysis demonstrates that *Chicou* waves are phase-locked with the tidal cycle during summer 2024, suggesting that the phenomenon may be predictable (Figure 18). However, in 2023, the temperature data at the wharf do not show any specific trend associated with the regular occurrence of *Chicou* waves observed with the camera (Figure 11). This may primarily be due to the greater distance of the waves from the wharf in 2023, which resulted in weaker temperature disturbances compared to 2024. Changes in stratification over fall 2023 may also have affected the intensity of the NLIWs. In addition, *Chicou* waves accounted for nearly half of the observed events in 2023, whereas in 2024 this ratio increased to 4/5.

Moreover, during our 2024 campaign, we observed that the *Chicou* waves appeared stronger during the spring tide. This observation is consistent with the findings of Pradhan et al. (2016) and Villamana et al. (2017), where internal waves carry more energy during spring tides. Based on our observations, this difference between neap and spring tide is not due to a change of stratification in 2024 (Figure 16). However, the transition to weaker stratification in 2023 as we moved from fall to winter may have influenced the intensity of *Chicou* waves, as said earlier. In order to predict the intensity of NLIWs accurately, additional long-term data are required, particularly to capture multiple *Chicou* waves during both spring and neap tides.

In the absence of such measurements, the satellite observations provide complementary insight into *Chicou* waves since 2016. The similar surface signature with the previously mentioned events suggests that the *Chicou* waves in Figure 15 are generated by the same mechanism. Moreover, the *Chicou* waves occur throughout the year, being observed in all seasons.

Moreover, in July 2021, another satellite image (Figure 19) clearly shows a cargo ship approaching the Grande-Anse terminal generating its own internal waves. A part of these internal waves seems to propagate in the wharf direction. This implies that the waves could catch up with the cargo during docking and potentially affect its maneuvering. This observation may support the hypothesis proposed by Grégorio et al. (2025), which suggests that ships may be affected by the internal waves they generate themselves.

Figure 19 – Sea-surface evidence of internal wavetrains being generated by a ship approaching the Grande-Anse Terminal on July 4, 2021. (Image source: Copernicus Sentinel-2 data).

The naturally generated NLIWs are susceptible to influencing marine operations. The observations of the *Colvert*, both near and further from the wharf, show current magnitudes from 0.5 $\mathrm{m\,s^{-1}}$ to 1 $\mathrm{m\,s^{-1}}$. However, due to divergent currents between the peak and the trough of NLIWs, differences can locally reach up from 1 $\mathrm{m\,s^{-1}}$ to 2 $\mathrm{m\,s^{-1}}$ (Figure 8 and Figure 10), which is significant enough to hinder marine operations such as docking. Indeed, according to the Recommendations of the Committee for Waterfront Structures, docking a cargo vessel such as the *Jaeger Arrow* (Dead Weight Tonnage around 24,000) is considered unfavourable at a docking velocity of 0.30 $\mathrm{m\,s^{-1}}$, and difficult in exposed locations like the Saguenay Fjord at 0.35 $\mathrm{m\,s^{-1}}$, according to the Permanent International Association of Navigation Congresses. Since docking velocities can safely reach 0.13 $\mathrm{m\,s^{-1}}$ (Roubos et al., 2017), the addition of NLIWs' currents of 1.0 $\mathrm{m\,s^{-1}}$ to this docking velocity could reach 3 times the 0.35 $\mathrm{m\,s^{-1}}$ limit if we consider the cargo as a particle following the current. Moreover, the depth of NLIWs is equivalent to, or approximately matches, the mid-draft of cargo vessels that dock near the wharf. The associated currents therefore act on a large portion of the ship's hull, which could hypothetically lead to lateral drift of the vessel during maneuvering.

It has already been demonstrated in Ueno (2003) that the wavelength and period of surface waves can influence a ship's drift speed. This suggests that, for future studies, it would be valuable to examine whether the NLIW wavelength plays a role relative to the ship's size, and how the NLIW period affects the ships's speed.

That said, no measurements of a cargo ship crossing an NLIW train while docking in this area have been collected, which prevents us from drawing definitive conclusions about the actual impact of NLIWs on docking maneuvers. Nevertheless, this hypothesis remains the most plausible, given the velocities generated by these waves and their regularity. Other phenomena were present, such as eddies and fronts near the wharf, but no ADCP data indicated that these fronts unrelated to NLIWs or the eddies could generate currents strong enough to interfere with docking maneuvers.

Credit author contributions

L. Hupé : Brought ideas; Writing; Created figures; Programmed; Implemented computer codes and supporting algorithms; Developed the methodology; Applied statistical, mathematical and computational techniques to analyze and synthesize study data; Conducted the research and investigation process; Data collection.

D. Bourgault: Brought ideas; Formulated research goals; Developed the methodology; Programmed; Implemented computer codes and supporting algorithms; Verified the overall reproducibility of results; Applied statistical, mathematical and computational techniques to analyze and synthesize study data; Conducted the research and investigation process, specifically field experiment preparation (logistics and instruments setup, configuration and tests) and data collection; Provided instrumentation; Managed activities to maintain research data for initial use and later reuse; Contributed to the writing of the initial draft (introduction and methodology sections); Critically reviewed and commented the initial drafts; Created Figure 15, Figure 17, Figure 18 and Figure 19; Oversight and led responsibility for the research activity planning and execution, including student supervision; Managed and coordinated responsibility for the research activity planning and execution; Acquired the financial support for the project that led to this publication.

S. Grégorio: Brought ideas; Formulated research goals; Developed the methodology; Programmed; Implemented computer codes and supporting algorithms; Verified the overall reproducibility of results; Applied statistical, mathematical and computational techniques to analyze and synthesize study data; Conducted the research and investigation process, specifically field experiment preparation (logistics and instruments setup, configuration and tests) and data collection; Critically reviewed and commented the initial drafts; Contributed to the writing of the initial draft (methodology section); Oversight and led responsibility for the research activity planning and execution, including student supervision.

C. Chavanne: Brought ideas; Formulated research goals; Participated in field experiment preparation and data collection; Provided instrumentation; Managed activities to maintain research data for initial use and later reuse; Critically reviewed and commented the initial drafts; Participated in the student supervision.

P. S. Galbraith: Brought ideas; Formulated research goals; Conducted the research and investigation process, specifically field experiment preparation (logistics and instruments setup, configuration and tests) and data collection; Provided instrumentation; Managed activities to maintain research data for initial use and later reuse; Managed and coordinated responsibility for the research activity planning and execution; Acquired the financial support for the project that led to this publication.

J. Lemelin: Implemented computer codes and supporting algorithms; student supervision.

CONCLUSION GÉNÉRALE

Les résultats de notre étude suggèrent que les ondes internes peuvent représenter un danger potentiel pour les opérations maritimes dans les zones côtières stratifiées, telles que le fjord du Saguenay. En effet, dans un cas idéalisé, les courants associés aux ondes internes pouvant atteindre 1 $\mathrm{m\,s^{-1}}$, additionnés à la vitesse d'accostage, excèdent les recommandations formulées dans Roubos et al. (2017). Les longueurs d'onde de 70 m et les périodes d'environ 1 minute observées dans les trains d'ondes ont aussi certainement une incidence sur la vitesse de dérive des cargos comme cela a été reporté pour les vagues de surfaces dans Ueno (2003). Cette étude a également pu appuyer l'hypothèse formulée dans Grégorio et al. (2025), selon laquelle un cargo peut être affecté dans sa manœuvre d'accostage par ses propres ondes internes. Cependant, l'accident du *Jaeger Arrow* étant un cas unique à ce quai, la combinaison de plusieurs facteurs ont certainement aidé à entraîner la collision (accostage deux heures après la marée haute, première tentative d'accostage échouée, absence de navire pilote). Néanmoins, les forts courants horizontaux associés aux ondes internes font de ce phénomène un risque naturel qu'il est essentiel de comprendre afin d'éviter d'éventuels accidents d'accostage. De plus, en l'absence de données *in-situ* au moment de l'accident, il n'est pas possible de confirmer si les ondes internes ont effectivement contribué à l'événement ce jour-là. De prochaines études sont nécessaires pour mesurer en conditions réelles la dérive d'un cargo engendrée par les ondes internes pendant ses manœuvres. Les données récoltées pourraient servir à la création d'outils utiles aux autorités portuaires pour mieux anticiper l'effet des ondes internes sur les manœuvres d'accostages.

RÉFÉRENCES

Alford, M.H., Peacock, T., MacKinnon, J.A., Nash, J.D., Buijsman, M.C., Centurioni, L.R., Chao, S.Y., Chang, M.H., Farmer, D.M., Fringer, O.B., et al., 2015. The formation and fate of internal waves in the South China Sea. Nature 521, 65–69.

Bergh, J., Berntsen, J., 2009. Numerical studies of wind forced internal waves with a nonhydrostatic model. Ocean Dynamics 59, 1025–1041.

Bourgault, D., 2008. Shore-based photogrammetry of river ice. Canadian Journal of Civil Engineering 35, 80–86.

Bourgault, D., Galbraith, P.S., Chavanne, C., 2016. Generation of internal solitary waves by frontally forced intrusions in geophysical flows. Nature communications 7, 13606.

Bourgault, D., Galbraith, P.S., Winkler, G., 2012. Exploratory observations of winter oceanographic conditions in the saguenay fjord. Atmosphere-ocean 50, 17–30.

Bourgault, D., Pawlowicz, R., Richards, C., 2024. g_rect: A MATLAB package for georectifying oblique images. Version v3.

Dunphy, M., Subich, C., Stastna, M., 2011. Spectral methods for internal waves: indistinguishable density profiles and double-humped solitary waves. Nonlinear Processes in Geophysics 18, 351–358.

Geyer, W.R., MacCready, P., 2014. The estuarine circulation. Annual review of fluid mechanics 46, 175–197.

Ghomsi, S.K., 2015. The analysis of shuttle-tanker and floating storage offloading during berthing operations at offshore Nigeria, in response to soliton and squall events. Ph.D. thesis. University of Abomey-Calavi, Cotonou, Republic of Benin.

Gong, Y., Xie, J., Xu, J., Chen, Z., He, Y., Cai, S., 2022. Oceanic internal solitary waves at the Indonesian submarine wreckage site.

Grégorio, S., Bourgault, D., Galbraith, P.S., Chavanne, C., Hupé, L., Richard, A., Landry, É., 2025. The impact of underwater waves on ship manoeuvrability: a case study in a fjord. Scientific Reports 15, 5598.

Grue, J., Bourgault, D., Galbraith, P.S., 2016. Supercritical dead water: effect of nonlinearity and comparison with observations. Journal of Fluid Mechanics 803, 436–465.

Heaps, N.S., Ramsbottom, A., 1966. Wind effects on the water in a narrow two-layered lake. Part i. Theoretical analysis. Part ii. Analysis of observations from Windermere. Part iii. Application of the theory to Windermere. Philosophical Transactions of the royal society of London. Series A, mathematical and physical sciences 259, 391–430.

Jackson, C.R., Apel, J., 2004. An atlas of internal solitary-like waves and their properties. Contract 14, 0176.

Jackson, C.R., Da Silva, J.C., Jeans, G., 2012. The generation of nonlinear internal waves. Oceanography 25, 108–123.

Klymak, J.M., Moum, J.N., 2003. Internal solitary waves of elevation advancing on a shoaling shelf. Geophysical Research Letters 30.

Lentz, S., Kirincich, A., Plueddemann, A., 2022. A note on the depth of sidelobe contamination in acoustic doppler current profiles. Journal of Atmospheric and Oceanic Technology 39, 31–35.

Osborne, A., Burch, T., 1980. Internal solitons in the Andaman Sea. Science 208, 451–460.

Osborne, A., Burch, T., Scarlet, R., 1978. The influence of internal waves on deep-water drilling. Journal of Petroleum Technology 30, 1497–1504.

Osborne, A.R., 2010. Internal waves and solitons. International Geophysics 97, 597–622.

Pawlowicz, R., 2003. Quantitative visualization of geophysical flows using low-cost oblique digital time-lapse imaging. IEEE journal of oceanic engineering 28, 699–710.

Pradhan, H.K., Rao, A., Joshi, M., 2016. Neap-spring variability of internal waves over the shelf-slope along western Bay of Bengal associated with local stratification. Natural Hazards 80, 1369–1380.

Richards, C., Bourgault, D., Galbraith, P.S., Hay, A., Kelley, D.E., 2013. Measurements of shoaling internal waves and turbulence in an estuary. Journal of Geophysical Research: Oceans 118, 273–286.

Richez, C., 1994. Airborne synthetic aperture radar tracking of internal waves in the Strait of Gibraltar. Progress in Oceanography 33, 93–159.

Roubos, A., Groenewegen, L., Peters, D.J., 2017. Berthing velocity of large seagoing vessels in the port of Rotterdam. Marine Structures 51, 202–219.

Stastna, M., Lamb, K.G., 2002. Large fully nonlinear internal solitary waves: The effect of background current. Physics of fluids 14, 2987–2999.

Thompson, D.R., Jensen, J., 1993. Synthetic aperture radar interferometry applied to ship-generated internal waves in the 1989 Loch Linnhe experiment. Journal of Geophysical Research: Oceans 98, 10259–10269.

Ueno, M., 2003. Experimental study on manoeuvring motion of a ship in waves, in: Proceedings of International Conference on Marine Simulation and Ship Maneuverability, 2003.

Villamana, M., Mouriño-Carballido, B., Maranón, E., Cermeno, P., Choucino, P., da Silva, J.C., Díaz, P.A., Fernández-Castro, B., Gilcoto, M., Graña, R., et al., 2017. Role of internal waves on mixing, nutrient supply and phytoplankton community structure during spring and neap tides in the upwelling ecosystem of Ría de Vigo (NW Iberian Peninsula). Limnology and Oceanography 62, 1014–1030.

Watson, G., Chapman, R., Apel, J., 1992. Measurements of the internal wave wake of a ship in a highly stratified sea loch. Journal of Geophysical Research: Oceans 97, 9689–9703.